MICROWAVE POWER COUPLER FOR A SUPERCONDUCTING MULTIPLE-CELL CAVITY FOR ACCELERATOR APPLICATION AND ITS TESTING PROCEDURES

BY

JIANJIAN LI

DEPARTMENT OF ELECTRICAL AND COMPUTER ENGINEERING

Submitted in partial fulfillment of the
requirements for the degree of
Doctor of Philosophy in Electrical Engineering
in the Graduate College of the
Illinois Institute of Technology

Approved _____
Adviser

Chicago, Illinois
December 2008

ACKNOWLEDGEMENT

I would like to thank my advisor, Dr. Thomas Wong, professor of Electrical and Computer Engineering (ECE) department at Illinois Institute of Technology (IIT), for his continuous encouragement, outstanding advising, and selfless help throughout my academic and research career at IIT. I also thank my supervisor, Dr. Nikolay Solyak, scientist of Technical Division at Fermi National Accelerator Laboratory (Fermilab) for his creative R&D solutions and helping me overcome obstacles I have encountered during the past several years at Fermilab.

Everyone in this project community has provided a friendly and enjoyable atmosphere for studying and working. Special thanks go to Andy Hocker, Elvin Harms, Tom Kubicki, Daniel Olis, Peter Prieto, Ivan Gonin, Andrei Lunin, Mark Champion, John Reid, Timergali Khabiboulline, Don Mitchell, Genfa Wu, Ping Wang, and Victor Yarba from Fermilab, USA and Wolf-Dietrich Moeller from DESY, Germany.

I would like to express my thanks to all committee members, Dr. Thomas Wong, Dr. Nikolay Solyak, Dr. Yongyi Yang, Dr. Yu Cheng, and Dr. Xiaofan Li, for their time of reviewing my thesis and valuable comments. Special thanks go to Dr. Jafar Saniie, associate chair and graduate program director of ECE department at IIT, for his final review of my thesis.

Thank US Department of Energy for funding my graduate education and research. Finally, I would like to thank my wife and newborn daughter for their continuous support.

TABLE OF CONTENTS

LIST OF TABLES

LIST OF FIGURES

Figure Page

Figure Page

Figure Page

LIST OF SYMBOLS

Symbol	Definition
c	Speed of Light in Vacuum
E_{acc}	Cavity Accelerating Gradient
E	Electric Field Intensity
G	Cavity Geometry Factor
H	Magnetic Field Intensity
I_b	Beam Current
I_{b0}	DC Beam Current
I_g	Generator Current
k	Thermal Conductivity
P_d	Cavity Dissipated Power
P_e	Cavity Emitted Power
P_r	Cavity Reflected Power
P_s	Cavity Stored Energy Change
P_t	Cavity Transmitted Power
Q	Heat Flux
$\overline{Q}$	Average Heat Flux
Q_0	Intrinsic Quality Factor
Q_e	External Quality Factor
Q_L	Loaded Quality Factor
R/Q	Cavity Shunt Impedance
R_c	Cavity Resistance
R_{th}	Conduction Thermal Resistance
$\tan\psi$	Detuning Angle
t_b	Beam Delay Time

Symbol	Definition
U	Cavity Stored Energy
V_{acc}	Accelerating Voltage
V_b	Beam-Induced Voltage
V_{cav}	Cavity Voltage
V_g	Generator Voltage
ω_0	Resonance Frequency
β_e	Coupling Coefficient
ϕ_b	Beam Delay Phase
ρ	Density of Material
δ	Skin Depth
σ	Electrical Conductivity
τ_L	Decay Time Constant

LIST OF ABBREVIATIONS

Abbreviation	Definition
CW	Continuous Wave
FEL	Free Electron Laser
FEM	Finite Element Method
Fermilab	Fermi National Accelerator Laboratory
FLASH	Free Electron Laser in Hamburg
HOM	Higher Order Mode
HTS	Horizontal Test Stand
IG	Ion Gauge
ILC	International Linear Collider
MP	Multipacting
OFHC	Oxygen Free High Conductivity
PMT	Photomultiplier
RF	Radio Frequency
RTD	Resistance Temperature Detector
SC	Superconducting
SLAC	Stanford Linear Accelerator Center
SS	Stainless Steel
SW	Standing Wave
TEM	Transverse Electromagnetic
Ti	Titanium
TIG	Tungsten Inert Gas
TiN	Titanium Nitride
TM	Transverse Magnetic
TW	Traveling Wave
VUV	Vacuum Ultraviolet

ABSTRACT

Superconducting cavity resonators offer the advantage of high field intensity for a given input power, making them an attractive contender for particle accelerator applications. Power coupling into a superconducting cavity employed in a particle accelerator requires unique provisions to maintain high vacuum and cryogenic temperature on the cavity side, while operating with ambient conditions on the source side. Components introduced to fulfill mechanical requirements must show negligible obstruction of the propagation of the microwave with absence of critical locations that may give rise to electron multipaction, leading to a multiple section design, instead of an aperture, a probe, or a loop structure as found in conventional cavities. A coaxial power coupler for a superconducting multiple-cell cavity at 3.9 GHz has been developed. The cavity is intended to be employed as an accelerator to provide enhanced electron beam quality in a free-electron laser in Hamburg (FLASH) user facility. The design of the coupler called for two windows to sustain high vacuum in the cavity and two bellows to accommodate mechanical dimensional changes resulting from cryogenics. Suppression of multipacting was accomplished by the choice of conductor dimensions and materials with low second yield coefficients. Prior to integration with the cavity, the coupler was tested for intrinsic properties in a back-to-back configuration and conditioned for high-power operation with increasing power input. Maximum incident power was measured to be 61 kW. When integrated with the superconducting cavity, a loaded quality factor of 9×10^5 was measured by transient method. Coupler return loss and insertion loss were estimated to be around -21 dB and -0.2 dB, respectively.

CHAPTER 1

INTRODUCTION

1.1 Particle Accelerators

Accelerator is a device or machine used to produce high-energy high-speed beams of charged particles, such as electrons, protons, or heavy ions, for research in high-energy and nuclear physics, synchrotron radiation source, Free Electron Laser (FEL), and certain industrial and medical applications. From the information obtained with the accelerators, physicists can determine the properties of the particles and their interactions. The higher the energy of the accelerated particles, the more closely we can probe the structure of matter. For that reason a major goal of researchers is to produce higher and higher particle energies.

Most particle accelerators can be divided into two types: circular accelerators and linear accelerators. In the circular accelerators, particles move in a circle until they reach sufficient energy. The particle track is typically bent into a circle using electromagnets. Figure 1.1 is a picture of Tevatron circular accelerator built at Fermi National Accelerator Laboratory (Fermilab). The advantage of circular accelerators over linear accelerators is that the ring topology allows continuous acceleration. Another advantage is that a circular accelerator is relatively smaller than a linear accelerator of comparable power. A linear accelerator would have to be extremely long to have the equivalent energy of a circular accelerator. Depending on the energy and the particle being accelerated, circular accelerators suffer a disadvantage in that the particles emit synchrotron radiation which is proportional to the fourth power of the particle energy and inversely proportional to the square of the radius of the path. It becomes the limiting factor on the final energy of

particles accelerated in the circular accelerator. The linear accelerator concept must be employed when extremely high energy is required. For this reason, many high energy particle accelerators are linear accelerators. A typical linear accelerator located at Stanford Linear Accelerator Center (SLAC) is shown in Figure 1.2. In linear accelerators, particles are accelerated in a straight line with a target of interest at one end. They are also used to provide an initial low-energy kick to particles before they are injected into circular accelerators.

Figure 1.1 Tevatron Circular Accelerator at Fermi National Accelerator Laboratory

Figure 1.2. A Linear Accelerator at Stanford Linear Accelerator Center

1.2 FLASH User Facility

Superconductivity is a phenomenon occurring in certain materials at low temperatures, characterized by exactly zero electrical resistance and the exclusion of the interior magnetic field. The power losses in the SC resonator walls are negligible and almost all the power can be transferred to the particle beam [3][1], which vastly reduces the energy consumed. In addition, the particle beam so created is of extremely high quality with small beam emittance growth in accelerating structures [64]. Thanks to their vanishing electrical resistance, the resonators can be made bigger than normally conducting designs because fewer interference fields arise. As a result, it is possible to produce a particle beam with a very small beam cross-section and high beam power. This means that a high collision rate for the accelerated particles can be achieved, which is the ideal prerequisite for new discoveries in particle physics. All of those make the SC approach an ideal choice for high energy accelerators [3].

FLASH which stands for "Free Electron Laser in Hamburg" is a Superconducting (SC) linear accelerator providing laser-like radiation in the Vacuum Ultraviolet (VUV) and soft X-ray range to various user experiments in many scientific fields. FLASH is also a pilot facility for the European X-ray FEL project and a test bed for further research and development for International Linear Collider (ILC) related SC accelerator technologies. Many scientific disciplines ranging from physics, chemistry and biology, material application, nuclear science, and medical diagnostics need a powerful X-ray source with pulse lengths in the femtosecond range. Such radiation of extreme intensity and

[1] Corresponding to references in the Bibliography.

adjustability over a wide range of wavelengths can be accomplished when using FLASH user facility.

FLASH is operated in the self-amplified spontaneous emission (SASE) mode and delivers sub-picosecond radiation pulses, with a wavelength range from 13 nm to 50 nm at gigawatt peak powers. In FLASH system the electron beam bunches are produced in a laser-driven photoinjector and accelerated by a 1.3 GHz SC linear accelerator, as shown in Figure 1.3. At intermediate energies of 125 and 450 MeV the 1 *nC* electron beam bunches are longitudinally compressed twice [23], thereby increasing the peak bunch current from initially 50-80 A to approximately 1000-2000 A as required for the FEL operation. Single pass high gain FEL requires long undulator systems. The FLASH undulator system consists of six modules with a length of 4.5 m each. The fixed gap is 12 mm with a peak magnetic field of 0.48 T realized with permanent NdFeB magnets. The undulator period is 27.3 mm. A pair of electromagnetic quadrupoles between each of the six modules provides a large acceptance in beam energy. Finally, a dipole magnet deflects the electron beam bunches into a dump, while the FEL radiation propagates to the experimental areas.

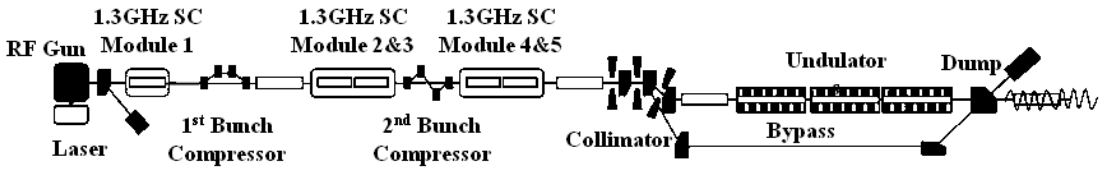

Figure 1.3. Structure of the FLASH User Facility

1.3 Third Harmonic SC Module

The design philosophy of producing electron beam bunches is based on using a long laser pulse to pull a long electron bunch from the photocathode. It is presently impossible to generate ultra-short and highly-charged bunches out of an RF gun exit because of the strong space charge coupling, especially at low energy levels. Therefore, in the 1.3 GHz accelerating SC module, the sinusoidal accelerating voltage profile distorts the long bunches [2]. Such distortion, if not corrected, sets a lower limit on the compression process and can thus significantly decrease the available peak bunch current.

For the FLASH linear accelerator, the electron beam bunch is accelerated on crest of the 1.3 GHz SC cavity voltage, V_{cav}, which is defined as the maximum accelerating voltage acting on a relativistic electron by integrating the electric field along the axis [57].

$V_{cav} = \int_0^L E(s)\exp(-i\omega s/c)ds$, where L is the cavity length, c is the speed of light in vacuum, s is the displacement, ω is the angular frequency, and $E(s)$ is electric field intensity on the axis.

The accelerating voltage in reality acting on long electron bunches is $V_{acc} = V_{cav}\cdot\cos(\omega t_b)\cdot\cos(\varphi)$ [57], where t_b is beam delay time and φ is the relative phase with respect to the electrons at the center of a beam bunch. Nonlinear distortion of accelerating voltage or energy distribution is introduced into the FLASH photoinjector system due to this sine-like voltage profile.

A 3.9 GHz third harmonic SC module was proposed to increase the peak bunch current of the electron beam and to linearize the accelerating voltage (energy distribution) acting on the electrons within a bunch in the longitudinal phase space for the FLASH

user facility [64]. A third harmonic module with four 3.9 GHz SC cavities will be installed downstream of the 1.3 GHz accelerating SC module 1, containing eight 1.3 GHz SC cavities. A schematic layout of the photoinjector for the FLASH user facility is shown in Figure 1.4. Installation of the third harmonic SC module will allow us to generate ultra-short and highly charged electron bunches with an extremely small beam emittance. Calculated results regarding the energy distribution within the bunch and the electron charge density are shown in Figure 1.5 and Figure 1.6. This innovative technology is essential to support a new generation of linear accelerators, electron colliders, and free electron lasers.

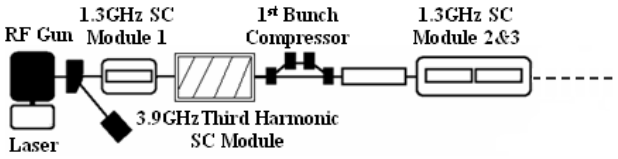

Figure 1.4. FLASH Photoinjector with Third Harmonic SC Module Installed

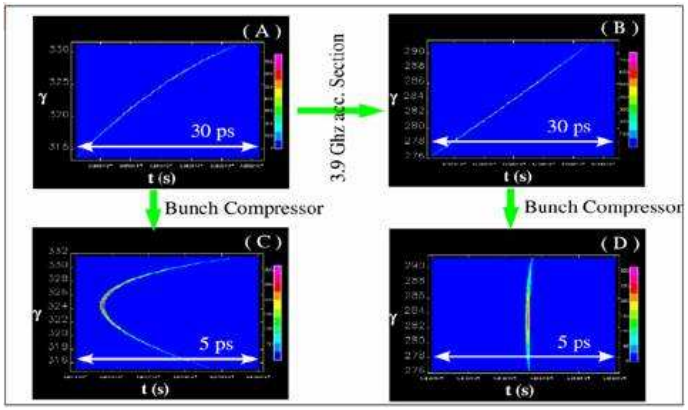

Figure 1.5. Energy Distribution of the Bunch before and after Bunch Compressor without (Left) and with (Right) the Installation of the Third Harmonic SC Module, calculated by P. Piot and W. Decking, Fermilab

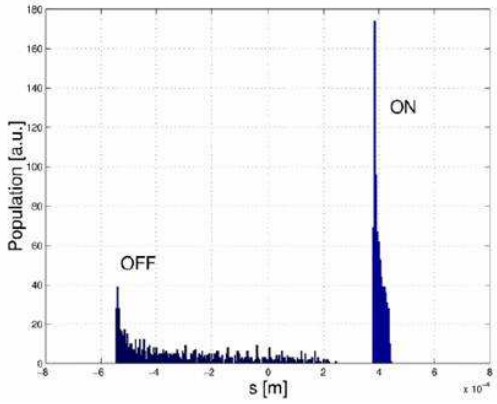

Figure 1.6. Comparison of the Electron Charge Density after the Bunch Compressor with the Third Harmonic SC Module On or Off, calculated by K. Floettmann, DESY, Germany

The long bunches are accelerated to an energy of about 180 MeV using a 1.3 GHz accelerating SC module 1. It is sufficient to consider the situation where the goal of the proposed SC module is to linearize the energy spread within the bunch which is accelerated on crest of the 1.3 GHz cavity voltage. The sum of the accelerating voltages from the two SC modules is

$V(s) = V_0 \cos(\omega_0 t) + V_1 \cos(\omega_1 t + \phi_1)$. s is relative displacement to the center of the bunch. V_0 is the accelerating voltage amplitude of the 1.3 GHz SC module 1 and V_1 is the accelerating voltage amplitude of the proposed SC module, which is operated at the frequency of ω_1 with the relative phase ϕ_1. Using the Taylor expansion at $t = 0$ of the sine and cosine functions, that is $\sin(\omega t) \approx \omega t$ and $\cos(\omega t) \approx 1 - (\omega t)^2 / 2$, one can rewrite equation as [57]:

$$V(s) = V_0 \cos(\omega_0 t) + V_1 \cos(\phi_1) \cos(\omega_1 t) - V_1 \sin(\phi_1) \sin(\omega_1 t)$$

$$V(s) \approx V_0 + V_1 \cos(\phi_1) - V_1 \omega_1 t \sin(\phi_1) - \frac{1}{2}(\omega_0 t)^2 (V_0 + V_1 (\frac{\omega_1}{\omega_0})^2 \cos(\phi_1))$$

The voltage is approximately constant within the bunch if the following conditions are met:

$$\phi_1 = -180^\circ \text{ and } V_1 = -(\frac{\omega_0}{\omega_1})^2 \frac{V_0}{\cos(\phi_1)}.$$

Under these conditions the sum of the accelerating voltages is constant (up to second order):

$$V(s) = V_0 - V_1 = V_0(1-(\frac{\omega_0}{\omega_1})^2).$$

It is important to note that it is the frequency ratio which determines the amplitude V_1 and total voltage amplitude. The normalized voltage $V(s)/V(0)$ is shown in Figure 1.7 for the comparison of three different scenarios: $\omega_1/\omega_0 = 3$ (third harmonic), $\omega_1/\omega_0 = 4$, and $\omega_1/\omega_0 = 2.3$. In all cases one can obtain a constant accelerating voltage within the bunch over a range of 2 mm and only small nonlinear deviations within a range of about 5 mm. After consideration of the required cavity voltage and the electromagnetic performance of the beam bunch we will consider the design of a 3.9 GHz third harmonic SC module which has medium cavity voltage requirement and medium beam performance for linearity compared to other two choices. As an example we consider eight 1.038 m long 1.3 GHz SC cavities operated at a gradient of 21.68 MV/m. The required cavity voltage amplitude and relative phase of the third harmonic module is equal to $V_1 = V_0/9 = 20$ MV and $\phi_1 = -180^\circ$, where $V_0 = 21.68 \times 1.038 \times 8 = 180$ MV and $\phi_0 = 0^\circ$. Four third harmonic SC cavities with a reasonably high accelerating gradient can provide total required gradient of 14.5 MV/m. The whole accelerating voltage with the consideration of 1.3 GHz and 3.9 GHz SC modules is actually the cumulative effect of

two sine-like accelerating voltages in the cavities the electron beam bunch has gone through.

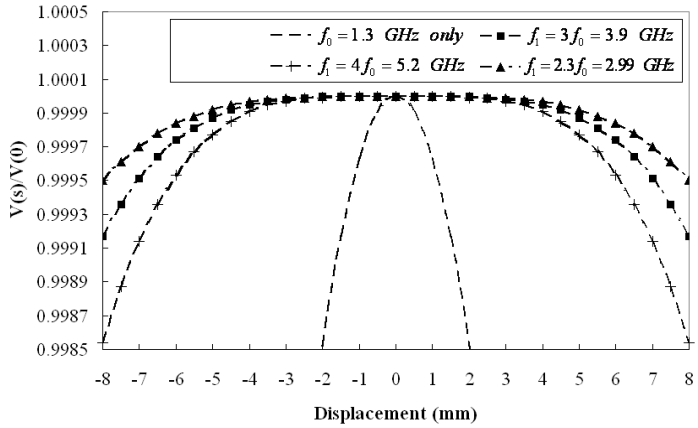

Figure 1.7. Total Normalized Accelerating Voltage with or without the Installation of the Proposed SC Module

CHAPTER 2

DESIGN CONSIDERATION

2.1 Design of Third Harmonic SC Cavity

Fermilab, as part of the FLASH collaboration, participates in developing, testing, and assembling the 3.9 GHz third harmonic SC cavities into a four-cavity SC module shown in Figure 2.1 for use at the FLASH user facility in DESY, Germany. This effort involves design, fabrication, testing, assembly, and eventual delivery of the module.

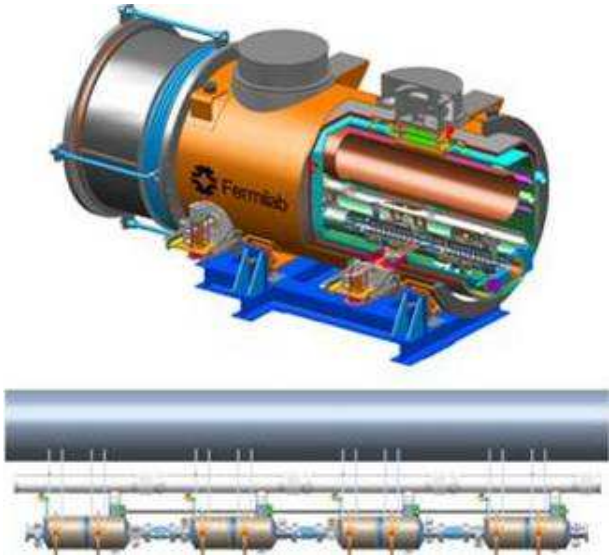

Figure 2.1. Third Harmonic SC Module (Top) and the Dressed Cavity String (Bottom) Inside the Module

Fermilab will provide a module containing four 3.9 GHz third harmonic SC cavities to be placed in the FLASH user facility. These cavities are TM_{010} structure designed to linearize the energy distribution of the 1.3 GHz accelerating SC cavities in this linear accelerator, thus providing improved longitudinal beam emittance. The

required operating gradient is 14.5 MV/m. Another goal of this project is to develop RF infrastructure at Fermilab by designing and assembling the necessary components including cryogenic module, qualified SC cavities, power couplers, Higher-Order-Mode (HOM) couplers, field probes, tuners, magnetic shielding, assembling tooling, vertical test stand, horizontal test cryostat, testing infrastructures, and shipping equipment for module transport to DESY, Germany.

Figure 2.2 shows a general microwave cavity used for electron acceleration. Assume an electron travels at the speed of light. This is a reasonable approximation for electron-positron accelerators with energies greater than 10 MeV. The charge enters an accelerating cavity on axis at time $t = 0$ and leaves at time $t = L/c$, L is the length of cavity each cell and c is the speed of light. During the transit, it sees a time-varying electric field. The time it takes the electron to transverse the cavity needs to be equal to one-half of an RF period for charge to receive the maximum kick from the cavity, that is, $\frac{L}{c} = \frac{\pi}{\omega_0}$, where ω_0 is the angular frequency of the accelerating mode.

To accelerate an electron beam, the longitudinal component of electric field must not vanish at the beam axis. Of all the Bessel functions, only J_0 satisfies this condition and all possible accelerating modes are of the type TM_{0np}. They are also called monopole modes [72] because of their field distribution. The TM_{010} mode is usually chosen for particle acceleration because it has the lowest eigen-frequency.

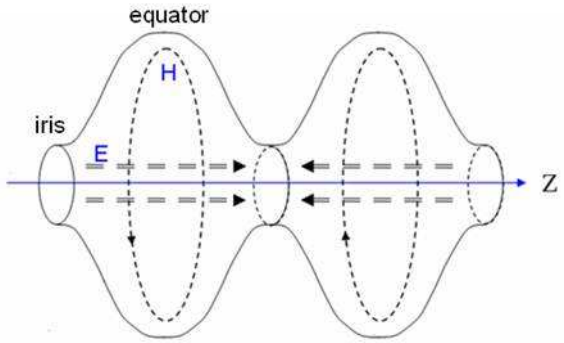

Figure 2.2. Field Vectors in an Elliptical Cavity Used for Particle Acceleration

The cavity built for the FLASH particle accelerator consists of nine elliptical-shape cells made of SC niobium. The main advantage of SC cavities is the extremely low surface resistance. The typical quality factor of normal conducting resonators is about 10^3 while for SC cavities it may exceed 10^9, thereby reducing the power losses by six orders of magnitude. SC cavities have been proved to operate at higher accelerating gradient, lower power demand, and more favorable beam accelerating conditions than traditional normal conducting resonators [5], [46], [52].

Figure 2.3 shows a 3.9 GHz third harmonic nine-cell cavity which is equipped with flange ports connecting to the power coupler (port 1), field probe (port 2), and two HOM couplers (port 3 and port 4). Field probe is a simple 50 Ω coaxial line and can be used to measure the field intensities and power decay constant at cryogenic temperature and vacuum environment. HOM couplers are designed to damp the harmful HOM powers induced by the electron beam. Klystron powers are electrically coupled to the cavity through the power coupler and the electromagnetic field is transformed from TEM wave to monopole TM_{010} wave in the cavity. The electric field map in the 3.9 GHz third

harmonic SC cavity with TM_{010} wave in each cell is shown in Figure 2.4. It should be noted that a phase difference of 180 (π) degrees occurs between adjacent cell boundaries, thus named the π mode.

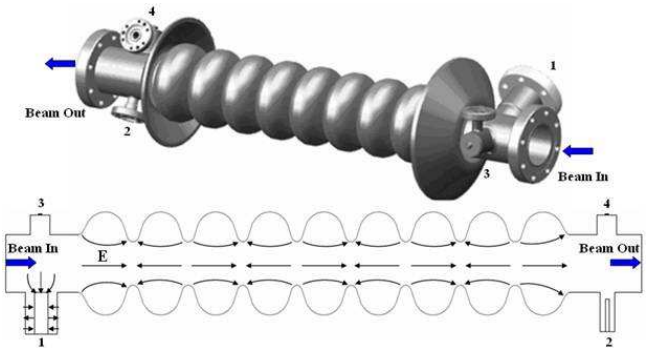

Figure 2.3. Electric Field Vectors in the Cavity (port 1: power coupler, port 2: field probe, port 3 and port 4: HOM couplers)

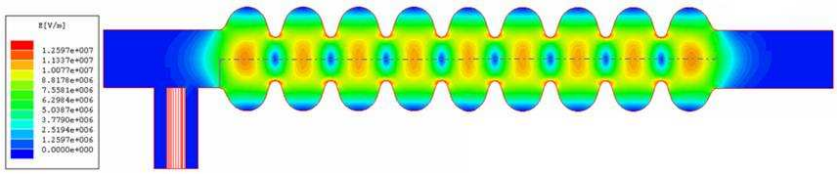

Figure 2.4. Electric Field Map for the Third Harmonic SC Cavity in π Mode

The design of third harmonic cavity has been revised to increase the coupling between power couplers and the cavity end cells. The iris radius of the end cell of the cavity has been increased to accomplish a better coupling. Regular cells have 30 mm iris diameter, while the end cell iris from the cavity tube side was increased up to 40 mm in diameter for better coupling with the power coupler and better damping of the HOM

waves, which can lead to bunch instabilities and beam breakup. Design parameters of the third harmonic SC cavities are shown in Table 2.1.

Table 2.1. Design Parameters of the Third Harmonic SC Cavities

Design Parameters	Values
Accelerating Structure	Standing Wave
Accelerating Mode	π Mode
Frequency	3.9 GHz
Cavity Length	0.3459 m
Number of Cells	9
R/Q	750 Ω
G Factor	275 Ω
Accelerating Gradient	14.5 MV/m
Stored Energy	2.5 J at 20 MV/m
E_{peak}/E_{acc}	2.26
B_{peak}/E_{acc}	4.84 mT/MV/m
B_{peak} at 20 MV/m	97 mT

2.2 Design Philosophy of Power Coupler

Power couplers for particle accelerators are among the most important and complicated components that interface with the accelerating SC cavities [11]. Power couplers for SC cavities must meet very strict requirements to perform at high power levels (at least tens of kilowatts) and in a variety of conditions (continuous wave, pulsed wave, traveling wave, and standing wave) without adversely affecting the performance of the cavities they are powering [11]. Producing excellent power coupler designs and achieving operational performances in particle accelerators are challenging tasks that

have involved large resources from many research laboratories and facilities [12]. The designs require state-of-the-art activities in RF, cryogenic and mechanical engineering, materials science, control theory, vacuum technology, and electromagnetic field modeling [6], [11], [12].

Recently, a lot of progress has been made to arrive at the successful design, construction, and operation of power couplers, as shown in bibliography. Simulations are now routinely performed for the prediction of electromagnetic, multipacting, and thermal properties of power couplers. From these studies, optimized designs have been achieved which can minimize potential problems ahead of final manufacture.

A power coupler can be considered as a properly designed transition in a perfectly matched transmission line, by which a properly determined amount of power can be delivered to the cavity and beam at a rate suitable for the specific application [11], as shown in Figure 2.5. Even though most power couplers do not make use of SC materials, the tight requirements imposed on them make the activities on power couplers as challenging as those for SC cavities. In addition, since any flaws of any component connected to the SC cavities can, and most likely will, degrade the cavity performance [12], the attention to the details of the design, fabrication, testing, and assembly of the power coupler is at least as important as that for the SC cavities themselves.

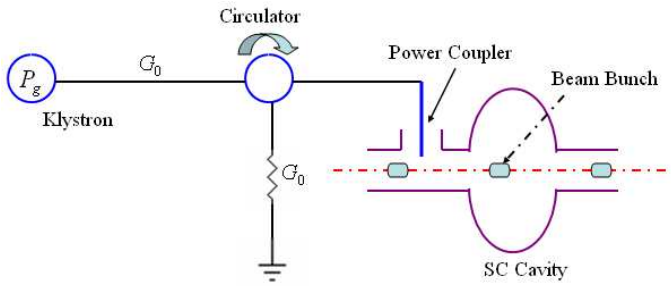

Figure 2.5. Schematic Diagram of Power Transfer Process

There are several primary functions associated with the power coupler design that we need to keep in mind [6], [11], [12].

- Efficiently transfer RF power to a load such as cavity and beam with minimum power reflection thus providing an impedance matching network.
- Serve as a vacuum barrier between an air-filled transmission line and extremely low pressures in cryogenic environment.
- Serve as a thermal transition from the room temperature to the cryogenic temperature (2 to 4.5 K) environment with low static and dynamic heat loads.
- Be multipactor-free or provide means such as biasing voltage, changing component geometry, or surface coating to suppress multipacting phenomenon or shift multipacting power levels.
- Support clean assembly procedures to minimize the risk of contaminating SC cavity.
- Provide adjustable options such as bellows design to minimize system thermal expansion or shrinkage effects.
- Some interlocks should be installed to prevent damage to the power coupler or even SC cavities during testing and operation.

2.2.1 Coaxial or Waveguide Power Coupler. Of all the possible geometries for coupling to SC cavities, two main choices have been adopted: coaxial and waveguide coupling. Waveguide coupling is conceptually simpler, since it does not require a transition between the power source and cavity. Due to the existence of a cutoff frequency in waveguides, the size of the waveguide coupler is generally larger at a given operating frequency than for the coaxial case.

Not being limited by a cutoff frequency, coaxial power couplers are in general more compact, especially for low frequency systems, and a variety of geometry and window arrangements are available to adapt to the specific need of the system. Only power density considerations and suppression of multipacting levels play a role in determining the geometry of coaxial power coupling system. The impedance of the coaxial line can be easily chosen to different values without modifying the coupler's outer dimensions to shift power levels at which multipacting may occur. A large range of coupling values can be achieved by proper insertion of the inner conductor into the cavity tube when necessary. In Fermilab's power coupler design, we adopt coaxial coupling approach to give us more design flexibilities to meet the system needs and design specifications.

2.2.2 Vacuum and Ceramic Window Requirements. Power couplers must perform as vacuum barriers between atmospheric pressure at room temperature and extremely low pressures in cryogenic environment. Windows are designed to separate the vacuum of the SC cavity from the atmospheric pressure of the transmission line. As electromagnetic

interfaces, they must satisfy strict matching requirements, so that power is reflected and dissipated only in minute quantities. Since dielectric materials are used for the construction of ceramic windows, the manufacturing techniques usually involve complicated interfaces of conductors, dielectrics, and brazing metals. The failure of a window in SC accelerator structures can necessitate very costly and lengthy repairs.

In addition, electronic phenomena at the windows can complicate the design. Multipacting at the windows can be particularly dangerous, as large amounts of power can be deposited in small areas of the dielectric, potentially leading to failure. In most cases ceramic windows are made from Al_2O_3 of 95% or higher purity. Because of its high secondary electron yield coefficient, coating with Titanium (Ti), Titanium Nitride (TiN) or other anti-multipactor materials is strongly recommended. In addition careful choice of window's geometry can mitigate this phenomenon. Exposure to radiation can also lead to charging phenomena at the window surface, leading to flashover of the accumulated charge and to damage of the window.

Windows can come in a circular waveguide configuration or in a variety of geometries adapted for coaxial lines. In some cases, double windows can guarantee vacuum property for whole system even if one window fails. In Fermilab's design two ceramic windows are used for the power coupler feeding the third harmonic SC cavities. Cylindrical cold window (close to power coupler cold end) can be assembled to the cavity under strict clean room conditions thus reducing the risk of cavity contamination. The circular warm window (close to power coupler warm end) is assembled after placing the cavity string into the vacuum vessel. With this enhanced design, a failure of one window does not need to immediately replace the power coupler and possibly the whole

module. All windows are TiN coated at least on vacuum side, which can dramatically minimize multipacting phenomenon and flashover activities occurring on the surface of the windows.

2.2.3 Thermal Transitions. As the RF power must be fed into the SC cavity, the power coupler must cross the boundary between room temperature RF transmission systems and the low-temperature SC cryogenic environment, usually 2 to 4.5 K, with or without dynamic heat load generated by the RF input power. This aspect of power coupler design imposes very tight requirements on geometries and very delicate balances between static and dynamic heat loads placed on the cryogenic system. The penetrations must be short due to the limited radial space available in most cryostat designs. Thus we must employ materials that can provide large thermal resistance to sustain large thermal gradients without introducing additional RF losses. In our design, inner and outer conductors are made of stainless steel which has a larger thermal resistance (smaller thermal conductivity) compared to the copper. To obtain better RF performance, all stainless steel components are copper plated on the vacuum side due to the larger electrical conductivity of copper (smaller surface resistance). Meanwhile intermediate thermal shields including 80 K and 4.5 K temperature fixed points are implemented in the design to minimize the total conduction and heat loads to cryogenic environment.

2.2.4 Bellows Selection. Most accelerators have adopted a fixed coupling approach, since the operational beam current is fixed and the beam loading is well defined. In Fermilab's power coupler design a fixed coupling option is adopted due to the constant

beam current (9 mA) input. Meanwhile power couplers must allow for some longitudinal motion inside the long SC module when the cavities are cooled down from room temperature to 2 K or warmed up to room temperature. For this reason, bellows in the inner and outer conductors of the coaxial line are implemented. The power coupler features a two-bellows design on the coaxial line to allow for tolerance adjustment and accommodate cavity motion during cool-down and warm-up of the cryostat.

2.2.5 Materials Selection. The third harmonic power coupler features two vacuum ceramic windows; one is a cylindrical cold window located near the SC cavity and thermally connected to the cryostat 80 K thermal shield and the other is a circular warm window mounted outside of the cryostat at room temperature. Both ceramic windows are coated with a thin layer of TiN for a lower secondary electron yield coefficient to suppress multipacting and discharging phenomena. The power coupler materials consist primarily of 316 Stainless Steel (SS), Oxygen-Free High Conductivity (OFHC) copper, Al_2O_3 ceramic (99.5% purity, TiN coated), and high purity copper plating. Joining techniques include brazing for the ceramic-to-metal and the stainless-to-copper joints, and welding for stainless-to-stainless and copper-to-copper joints. The inner conductor attachment to the cold window assembly requires for electron beam welds. The outer conductor attachment relies on Tungsten Inert Gas (TIG) welding in an oxygen-free chamber filled with helium and argon.

2.2.6 Interlocks Installation. The operation of high power couplers must include adequate protection and monitoring that prevent pressures from reaching the discharge

limit; that prevent overheating of the power coupler, especially with regard to the windows themselves; that monitor arcing that can occur at any location within the power coupler vacuum; and that monitor the electron current near the ceramic windows. The power couplers in this design have been equipped with different kinds of sensors to monitor the conditioning effect and to act as interlocks. Vacuum gauges are most commonly used, detecting the air pressure in system. Small coaxial electron pickups will detect electron current. Photomultipliers (PMT) will sample light effects. Resistance Temperature Detectors (RTD) can measure the window's temperature.

2.3 Structure of the 3.9 GHz Power Coupler

The team at Fermilab has researched and developed a new 3.9 GHz power coupler for third harmonic SC cavities after a series of calculations of different power coupler designs and considerations of electromagnetic, coupling, multipacting, thermal, mechanical, and material properties. Compared with the 1.3 GHz power coupler for the FLASH linear accelerating module, a lot of critical improvements have been made to the 3.9 GHz power coupler. It is the first time to use two ceramic windows to enhance the vacuum level for the entire system and prevent cavity against contamination. With this enhanced design, a failure of one window does not necessitate the immediate shut down of the RF module. Two coaxial-bellows sections were designed together to allow for tolerance adjustment and to accommodate cavity expansion or contraction due to temperature change of the cryostat while still providing a very low power reflection if careful selection of the separation distance between the two bellows sections. Unlike the 1.3 GHz power coupler using a DC field applied to the inner conductor to suppress the

multipacting activity, no multipacting was found for the 3.9 GHz power coupler due to the dimensional changes and use of the materials with a low secondary yield coefficient. Meanwhile, heat loads transferring to the cryogenic environment were kept lower than that for the 1.3 GHz system due to the introduction of the two thermal shields with constant temperatures.

This is a 50 Ω coaxial line with a 30 mm diameter of outer conductor. For the cold window, we adopted the cylindrical ceramic window with TiN coated to reduce the secondary electron yield coefficient. For the warm window, we are using a waveguide circular window with excellent RF performance at 3.9 GHz frequency. We also applied a two-bellows design for obtaining more mechanical flexibilities. Hollow coupler tip (cold end) can help to reduce the mechanical stress on cold window area. The simulations did not show any multipacting activities in the power coupler and third harmonic SC cavity structures during all possible power ranges. All components of the power coupler, including cold window, warm window, bellows section, waveguide-to-coax transition, and vacuum and diagnostic ports were optimized by high frequency simulation software HFSS for low power reflection at the operating frequency. Static and dynamic heat loads at 80 K and 4.5 K thermal shields for copper plated stainless steel tubes and bellows have been analyzed in ANSYS with different RF input power levels. Detailed layout and design parameters of the power coupler are shown in Figure 2.6, Figure 2.7, and Table 2.2, respectively.

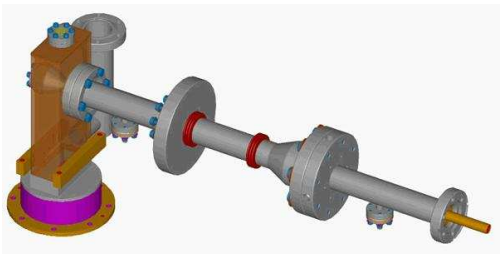

Figure 2.6. Diagram of the 3.9 GHz Power Coupler

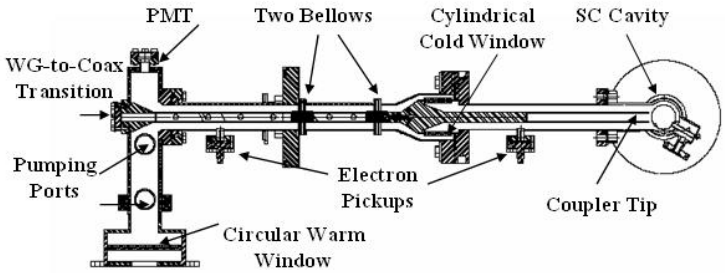

Figure 2.7. General Layout of the 3.9 GHz Power Coupler

Table 2.2. Main Features of the 3.9 GHz Power Coupler

Parameters	Values
Frequency	3.9 GHz
Pulse Length	1.3 ms
Repetition Rate	5 Hz
Incident Power	9.26 kW at $Q_e=9\times10^5$
Type	Coax
Window	Cylindrical and Circular
Impedance	50 Ω
Bellows	Two Bellows
Copper Plated	All SS and Bellows
Waveguide	WG284

The power coupler consists of a “cold part” which is mounted on the SC cavity in the clean room and closed by a ceramic cylindrical window, and a “warm part”, which is assembled after installation of the cavity in the SC module, as shown in Figure 2.8. The warm part contains the transition from rectangular waveguide to coaxial line. This part is evacuated and sealed against the air-filled waveguide by a second ceramic window. The elaborate two-window solution was chosen to get maximum protection of the SC cavity against contamination during mounting in the module and against window fracture and vacuum leakage during testing and operation.

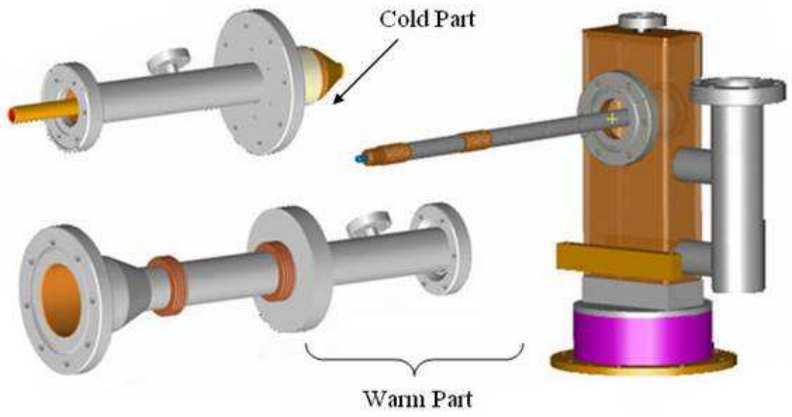

Figure 2.8. Warm Part and Cold Part Configuration of the Power Coupler

CHAPTER 3

RF DESIGN AND MODELING

3.1 RF Simulation of Coupler Subcomponents

Finite Element Method (FEM) electromagnetic modeling programs such as HFSS and Microwave Studio have been used to evaluate the field distributions in SC cavities, power couplers, and transitions and improve the impedance matching at windows, bellows section, and waveguide-to-coax transition [15], [40], [43], [59]. It must be done to ensure proper power transfer and minimize standing waves in the components. The FEM is a numerical technique for finding approximate solutions of the classic Maxwell's equations. The solution approach is based on rendering the partial differential equations into an approximating system of ordinary differential equations, which are then numerically integrated using standard techniques such as Euler's method or Runge-Kutta method, etc.

It is preferable to locate the power coupler for a SC cavity just outside the end cell instead of inside the cell to reduce the risk of thermal breakdown or field emission of the cavity itself. Figure 3.1 shows the electric field vectors in the coupling area of the power coupler and the first three cells of the third harmonic SC cavity. Power is coupled to the cavity through a coaxial power coupler and the electromagnetic field is transformed from TEM wave to TM_{010} wave in π mode. Structure layout of the power coupler is shown in Figure 3.2.

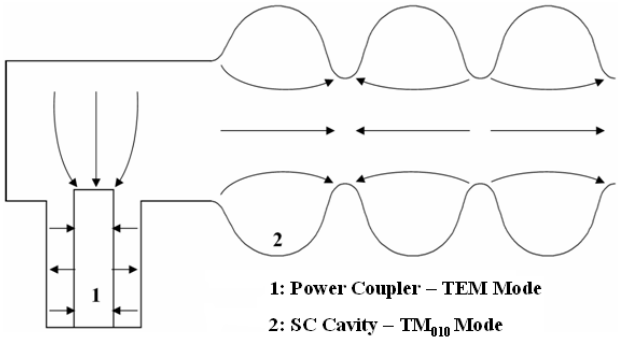

Figure 3.1. Electric Field Vectors in the Coupling Area

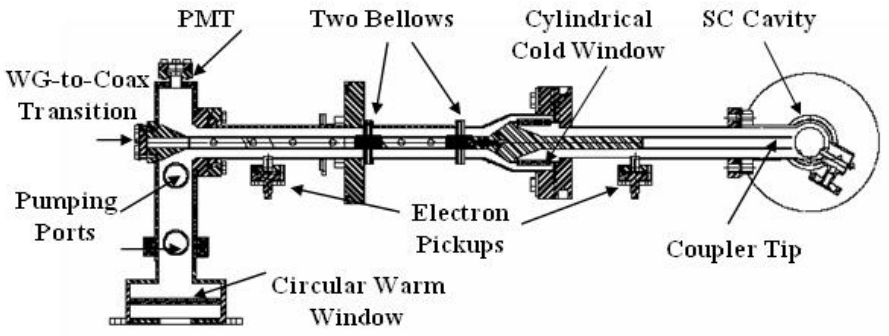

Figure 3.2. Detailed Layout of the Power Coupler

3.1.1 Cylindrical Cold Window. The cylindrical cold window operated at 80K degree shown in Figure 3.3 is made of alumina (Al2O3) with a dielectric constant of 9.8 and can be easily adapted for coaxial lines. From RF simulation we find that the reflection coefficient is very sensitive to the length of A. Careful selection of A is important to obtain an excellent RF performance of cold window. After optimization, the S11 parameter is limited to 0.027 when A is equal to 10 mm. S11 parameter curve is shown in Figure 3.4. Field maps are shown in Figure 3.5. All field maps shown in this thesis are calculated and plotted for an incident power of 1 W.

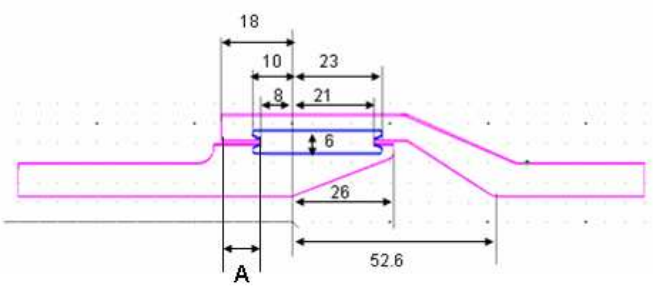

Figure 3.3. Geometry of the Cylindrical Cold Window

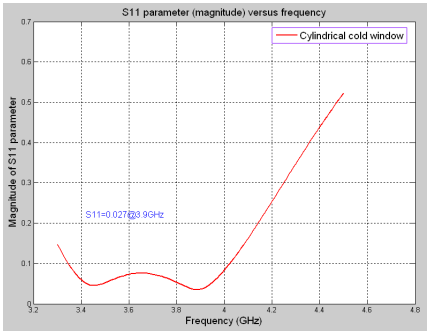

Figure 3.4. S_{11} Parameter Curve of the Cold Window

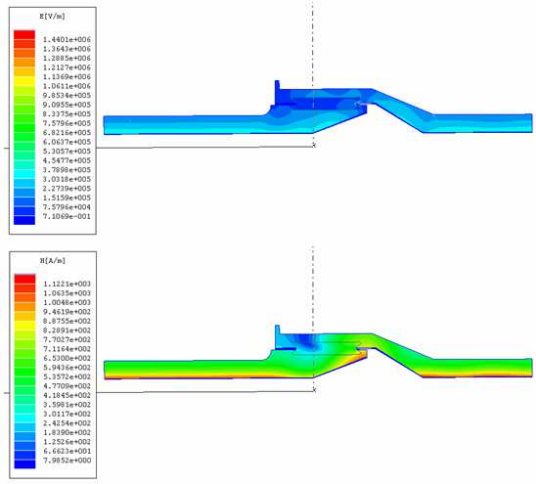

Figure 3.5. Electric and Magnetic Fields of the Cold Window

3.1.2 Two Bellows Sections. Two coaxial-bellows sections were designed together to allow for tolerance adjustment and to accommodate cavity expansion or contraction due to temperature change of the cryostat. At first, only one bellow section was put in the design, but the power reflection was relatively high even though various shapes and numbers of convolutions were tried. It was found that the power reflection could be substantially reduced if two bellow sections separated by odd integer multiple of quarter wavelength were employed. In this way, the reflected waves from the two bellows sections are made to cancel each other at the input port. S_{11} is equal to 0.002 at 3.9 GHz in this refined configuration, as shown in Figure 3.6. The field map is shown in Figure 3.7. Almost no standing wave regime may exist between the two bellows sections.

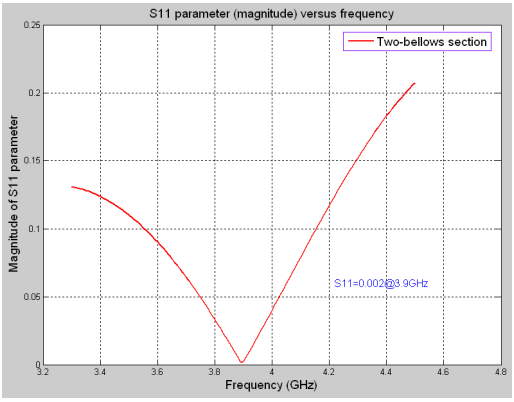

Figure 3.6. S_{11} Parameter Curve of the Two-Bellows Sections

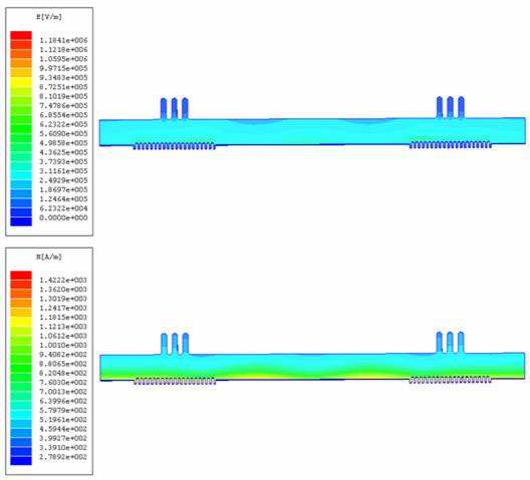

Figure 3.7. Electric and Magnetic Fields of the Two-Bellows Sections

3.1.3 Waveguide-to-Coax Transition. A waveguide-to-coax transition must be applied to connect the klystron output and the coaxial power coupler. A door-knob design has been adopted to meet this requirement, as shown in Figure 3.8. The field mode at 3.9 GHz is transformed from TE_{10} wave in the rectangular waveguide to the TEM wave in coaxial line. S_{11} parameter shown in Figure 3.9 is equal to 0.0025 at 3.9 GHz with two pumping ports installed in the waveguide. Field maps are shown in Figure 3.10.

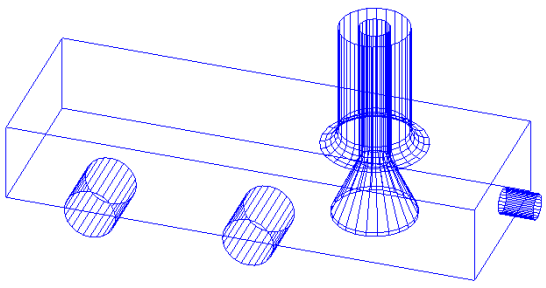

Figure 3.8. Diagram of the Waveguide-to-Coax Transition

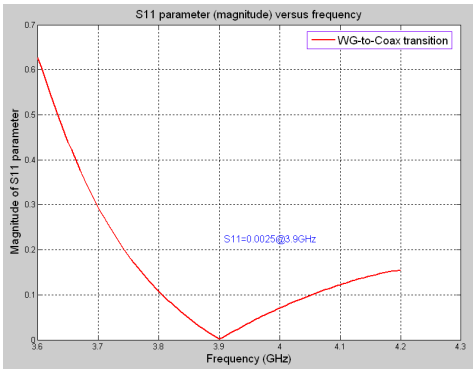

Figure 3.9. S_{11} Parameter Curve of the Waveguide-to-Coax Transition

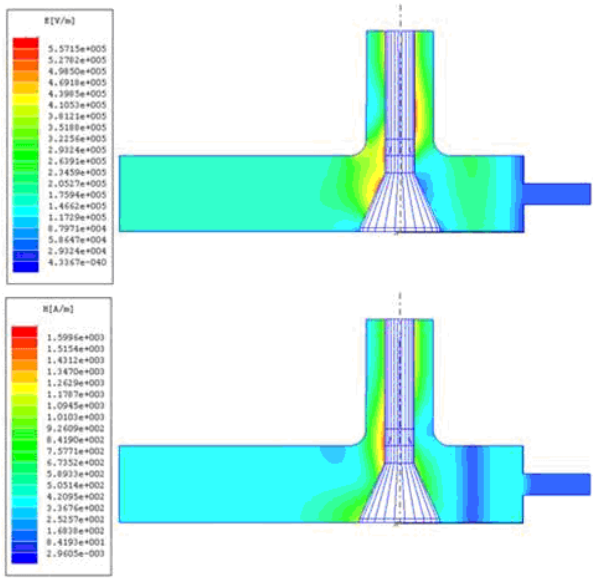

Figure 3.10. Electric and Magnetic Fields of the Waveguide-to-Coax Transition

3.1.4 Circular Warm Window. A circular warm window operated at room temperature with two waveguide openings on both sides shown in Figure 3.11 can be easily implemented into the rectangular transmission line just before the waveguide-to-coax transition. Circular warm window is designed and fabricated by an industrial company, CPI. The warm window is made of high purity alumina with a dielectric

constant of 9.2. Comparison of the S_{11} parameters calculated by CPI and at Fermilab is shown in Table 3.1. Reflection coefficient can be reduced to 0.03 at 3.9 GHz operating frequency as shown in Figure 3.12.

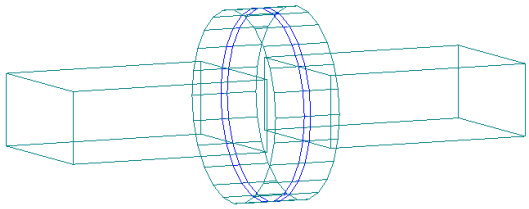

Figure 3.11. Diagram of the Circular Warm Window

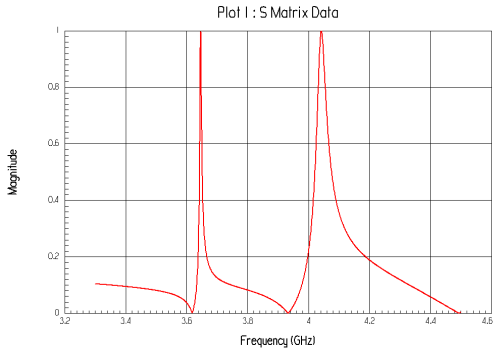

Figure 3.12. S_{11} Parameter Curve of the Warm Window

Table 3.1. S Parameters Calculated by CPI and at Fermilab

S Parameters	CPI	Fermilab
S_{11}	0.024	0.0336
VSWR	1.05	1.07
Return Loss	-32.4 dB	-29.5 dB

3.2 High-Power Test Stand

It is important for the power couplers to be tested with high power prior to the assembly on a SC cavity cryostat since any flaws or contamination of the power couplers can degrade the cavity performance. Two power couplers will be assembled in back-to-back arrangement with their probes connected by a waveguide transition on a test stand shown in Figure 3.13. Our design can enable maximum power transfer between power couplers in waveguide (S_{11}=0.0085). S_{11} parameter and field maps are shown in Figure 3.14 and Figure 3.15.

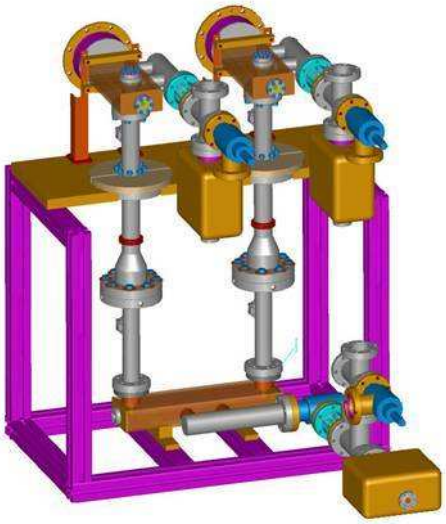

Figure 3.13. General Layout of the High-Power Test Stand

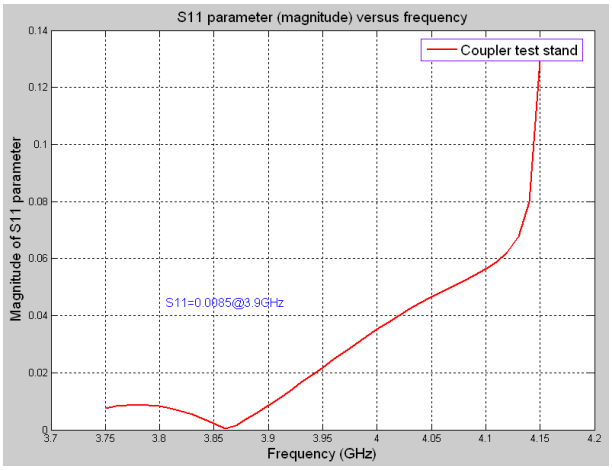

Figure 3.14. S_{11} Parameter Curve of the Test Stand

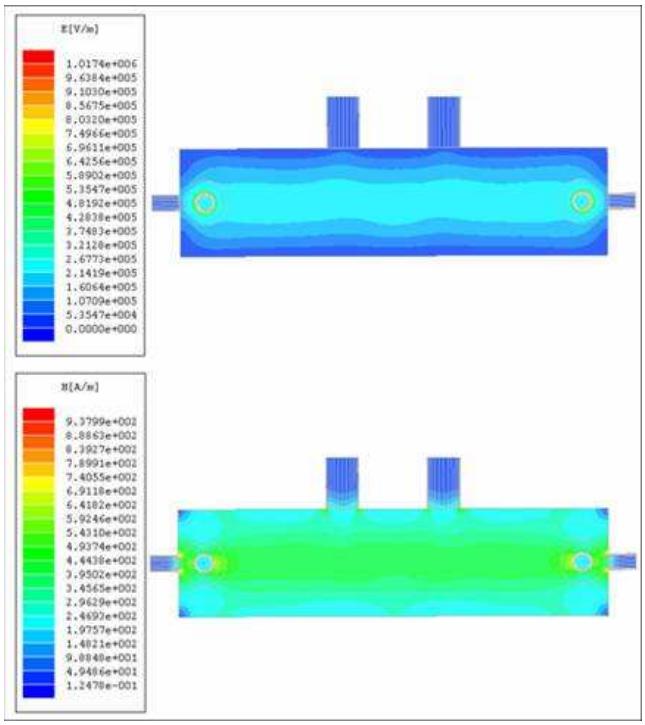

Figure 3.15. Electric and Magnetic Fields in Waveguide Transition of the Test Stand

3.3 Simulation of Full Geometry

The structure of the power coupler is quite complicated as discussed earlier. All parts including cylindrical window, circular window, bellows section, waveguide-to-coax transition, and diagnostic ports were optimized for low power reflection and dissipation at the operating frequency. Finally full geometry was simulated to check the resulting return loss, insertion loss, and field distributions. After careful selection of the geometry and the materials, the return loss was reduced to -21 dB and the insertion loss was only -0.2 dB, respectively, as shown in Figure 3.16. Plane AA', to which the return loss is referred in Figure 3.17 is the input port of the waveguide tube. The insertion loss was calculated between plane AA' and plan BB' which also served as an interface for the power coupler and the cavity. It is obvious that both windows are placed in the locations with low amplitudes of electric fields according to Figure 3.17. As a result, the risk of excessive electromagnetic heating, voltage breakdown, and multipacting phenomena for the windows is minimized.

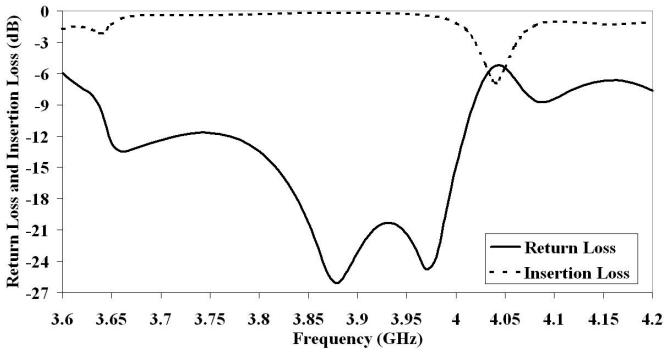

Figure 3.16. Return Loss and Insertion Loss Curves of the Power Coupler

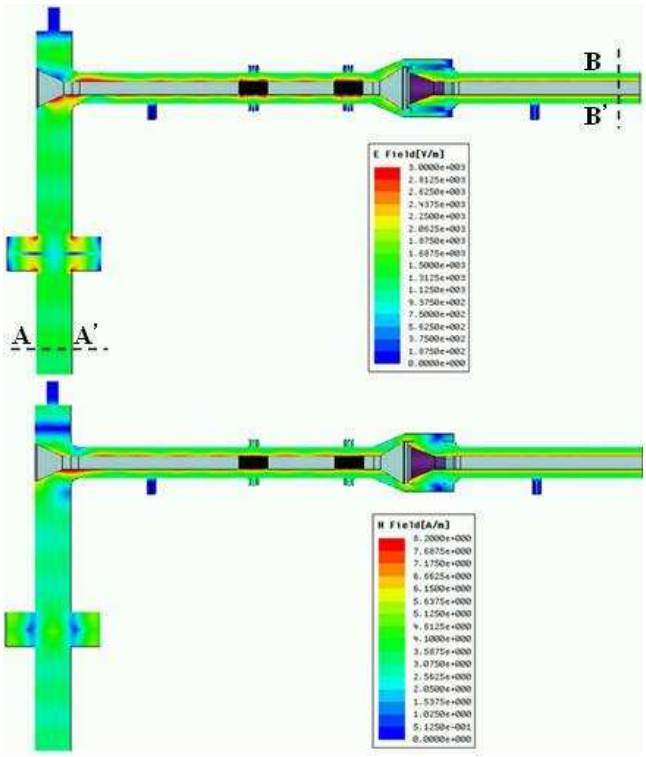

Figure 3.17. Electric and Magnetic Fields of the Power Coupler

CHAPTER 4

COUPLING OF POWER TO THE CAVITY

4.1 Model of Equivalent Circuits

Power measurements without beam load are necessary methods for predicting SC cavity and power coupler performance before the operation of accelerating particle beams [1]. To predict the performance more accurately, a second order differential equation by modeling a series of lumped equivalent circuits is created to represent this one-port RF coupling system. Some equations are also developed for power calculations at steady state and transient state. It is necessary to understand and control the cavity and power coupler behavior during testing and operation [7], [39], [54]. First, the RF coupling system equivalent circuit model is set up, and the relation between the parameters of the cavity and the equivalent circuit is introduced. Then the differential equations for the coupling system working in steady state are derived. Finally, the transient state equations are obtained for pulsed power calculations by solving this differential equation for the equivalent circuit with specific boundary conditions.

In general, a third harmonic SC cavity is equipped with one power coupler, one field probe, and two HOM couplers. The power coupler supplies the RF power to the cavity. RF signal picked up from field probe is used to detect the field frequencies, intensities, and to calculate the accelerating gradient in the cavity from the time constant factor. HOM couplers are used to extract the harmful HOM power induced by the particle beam. The coupling strength of the field probe and HOM couplers at the fundamental frequency of 3.9 GHz is very weak and can be neglected in the equivalent circuit model. A third harmonic SC cavity assembled with a power coupler operating at 3.9 GHz is

shown in Figure 4.1. Diagram of the power delivery process is shown in Figure 4.2. Between the klystron and the power coupler is an isolator which ensures that power reflecting from the cavity is terminated in a matched load. Good isolation is necessary since the klystron may be destroyed by the reflected power. The equivalent circuit of the entire coupling system without beam loading is shown in Figure 4.3. In this calculation only ohmic loss due to the cavity surface resistance is considered. It is noted that additional losses from electron field emission and cavity quench may be induced into the system at very high accelerating gradients. At the system nominal value of 14.5 MV/m accelerating gradient, we only consider the effect of ohmic loss with a good approximation for the coupling system.

Figure 4.1. Third Harmonic SC Cavity Equipped with a Power Coupler

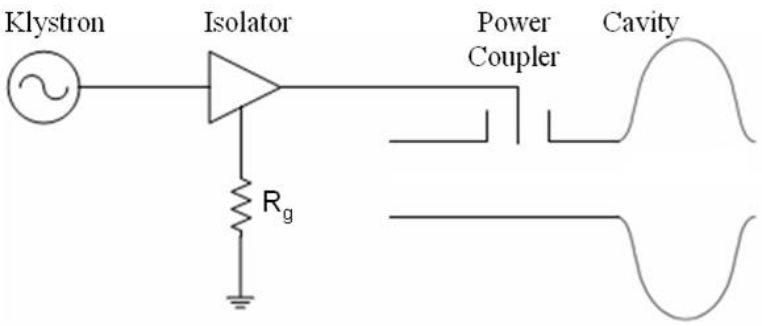

Figure 4.2. Diagram of the Power Delivery Process

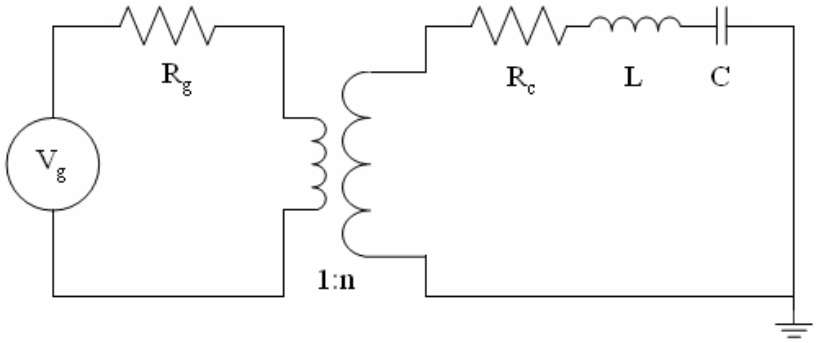

Figure 4.3. Equivalent Circuit Model of the Coupling System

The klystron and isolator combination is modeled by an ideal voltage source V_g with a serial resistor R_g. Cavity in resonant mode can be equivalently described by means of a serial RLC circuit, where R_c, L, C are the resistance, inductance, and capacitance of the SC cavity [1]. The power coupler is modeled by a voltage transformer with a turns ratio of 1 to n.

The cavity voltage is defined as $V_c = \frac{|I|}{\sqrt{2} \cdot \omega_0 C} = d \cdot E_{acc}$. Here d is the effective cavity accelerating length, E_{acc} is the cavity accelerating gradient, and $|I|$ is the

amplitude of circuit current I. Generally, the cavity's intrinsic parameters are defined at the cavity resonance frequency ω_0.

The cavity emitted power P_e and dissipated power P_d are $P_e = \frac{n^2 R_g |I|^2}{2}$ and $P_d = \frac{R_c |I|^2}{2}$. The cavity stored energy at ω_0 is $U = \frac{L|I|^2}{2} = \frac{CV_c^2}{2} = \frac{|I|^2}{2\omega_0^2 C}$. The external quality factor of the RF coupling system is $Q_e = \frac{\omega_0 U}{P_e} = \frac{\omega_0 L}{n^2 R_g} = \frac{1}{\omega_0 C n^2 R_g}$. The cavity intrinsic quality factor is $Q_0 = \frac{\omega_0 U}{P_d} = \frac{\omega_0 L}{R_c} = \frac{1}{\omega_0 C R_c}$, $\omega_0 = \frac{1}{\sqrt{LC}}$.

The power coupler coupling coefficient is defined as $\beta_e = \frac{Q_0}{Q_e} = \frac{P_e}{P_d} = \frac{n^2 R_g}{R_c}$. And the loaded quality factor Q_L for the whole coupling system is $\frac{1}{Q_L} = \frac{1}{Q_0} + \frac{1}{Q_e}$ or $Q_L = \frac{\omega_0 L}{R_c + n^2 R_g} = \frac{Q_0}{1+\beta_e}$.

The cavity shunt impedance R is defined as: $R = \frac{V_c^2}{P_d} = \frac{1}{R_c \omega_0^2 C^2}$ and $\frac{R}{Q} = \frac{R}{Q_0} = \frac{1}{\omega_0 C} = \omega_0 L$ [1]. Normally the R/Q is the cavity instinct parameter which can be determined by the cavity geometrical structure from FEM simulations. Based on above equations, the equivalent circuit parameters of the SC cavity can be expressed as:

$$C = \frac{1}{(R/Q)\omega_0},\ L = \frac{(R/Q)}{\omega_0}, \text{ and } R_c = \frac{\omega_0 L}{Q_0} = \frac{(R/Q)}{Q_0}.$$

In the circuit shown in Figure 4.3, the differential equation based on Kirchhoff current law relating current I and generator voltage V_g is [1]:

$$L\frac{dI}{dt}+(n^2R_g+R_c)I+\frac{1}{C}\int Idt=nV_g \text{, that is}$$

$$L\frac{dI^2}{dt^2}+(n^2R_g+R_c)\frac{dI}{dt}+\frac{I}{C}=n\frac{dV_g}{dt}$$

At steady state, the generator voltage can be written as $V_g=V_0\exp(i\omega_0 t)$. Substituting V_g into this main equation, the current I at resonance frequency is solved as

$$I=\frac{nV_g}{R_c(1+\beta_e)}=\frac{nV_0}{R_c(1+\beta_e)}\cdot\exp(i\omega_0 t).$$

The incident power, what the cavity can obtain from the generator, is $P_i=\frac{|V_g|^2}{8R_g}=\frac{V_0^2}{8R_g}$. According to the definition, the cavity dissipated power is

$$P_d=\frac{R_c|I|^2}{2}=\frac{4\beta_e P_i}{(1+\beta_e)^2}.$$

The cavity emission power is $P_e=\frac{n^2R_g|I|^2}{2}=\frac{4\beta_e^2P_i}{(1+\beta_e)^2}=\beta_e P_d$. Then the cavity accelerating gradient can be written as $E_{acc}=\frac{|I|}{\sqrt{2}\cdot d\omega_0 C}=\sqrt{\frac{4\beta_e(R/Q)Q_L P_i}{d^2(1+\beta_e)}}$ and the reflected power is $P_r=P_i-P_d$.

If the incident power is pulsed wave, the cavity is working under a transient state at the pulse start and end periods. For a standard square wave pulse, the generator voltage $V_g=V_0\exp(i\omega_0 t)$ after the RF power switch on, and $V_g=0$ after the RF power switch off. The circuit current during RF power switched on becomes [1],

$$I = \frac{nV_g}{R_c(1+\beta_e)}\left[1-\exp\left(-\frac{\omega_0}{2Q_L}t\right)\right] = \frac{nV_0}{R_c(1+\beta_e)}\left[1-\exp\left(-\frac{\omega_0}{2Q_L}t\right)\right]\cdot\exp(i\omega_0 t).$$

Then the cavity accelerating gradient can be written as

$$E_{acc} = \frac{|I|}{\sqrt{2}\cdot d\omega_0 C} = \sqrt{\frac{4\beta_e(R/Q)Q_L P_i}{d^2(1+\beta_e)}}\left[1-\exp\left(-\frac{\omega_0}{2Q_L}t\right)\right].$$

The cavity stored energy change is $P_s = \frac{1}{2}L\frac{d(|I|^2)}{dt}$ and the reflected power is $P_r = P_i - P_d - P_s$.

After switching RF power off after a duration of pulse length τ_0, the main differential equation becomes

$$L\frac{dI^2}{dt^2} + (n^2R_g + R_c)\frac{dI}{dt} + \frac{I}{C} = 0.$$

The boundary conditions for this transient state are $I(t\to\infty) = 0$ and $I(\tau_0) = \frac{nV_0\cos(\omega_0\tau_0)}{R_c(1+\beta_e)}\left[1-\exp\left(-\frac{\omega_0}{2Q_L}\tau_0\right)\right]$. Then, the circuit current I is obtained as $I = I(\tau_0)\exp\left[-\frac{\omega_0}{2Q_L}(t-\tau_0) - i\omega_0(t-\tau_0)\right]$ and the reflected power becomes $P_r = -P_d - P_s = P_e$.

Analytic solutions including dissipated power, stored energy change, reflected power, and emitted power for the pulse length of 1300 μs at different loaded quality factors are graphically shown in Figure 4.4, Figure 4.5, and Figure 4.6. To maintain a 14.5 MV/m accelerating gradient, the required power from the generator is ranging from 5 kW to 15 kW, depending on the system's loaded quality factors. At first, most power is reflected during the filling stage of the cavity. After then, the reflected power will pass

through the zero level and reaches its nonzero steady-state level which is almost equal to the incident power. When the klystron is abruptly turned off, the reflected power is just equal to the emitted power and exponentially decreased to zero.

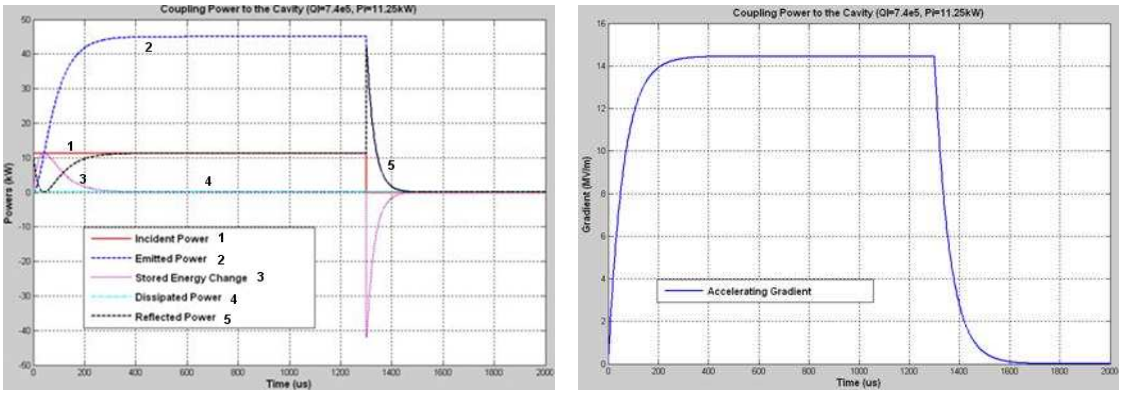

Figure 4.4. Power Level and Accelerating Gradient Curves at $Q_L = 7.4\times10^5$ and Incident Power of 11.25 kW

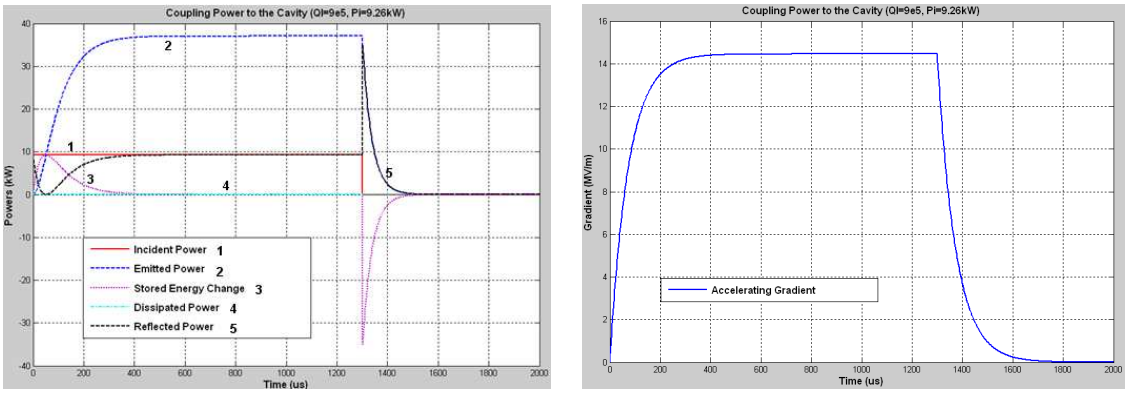

Figure 4.5. Power Level and Accelerating Gradient Curves at $Q_L = 9\times10^5$ and Incident Power of 9.26 kW

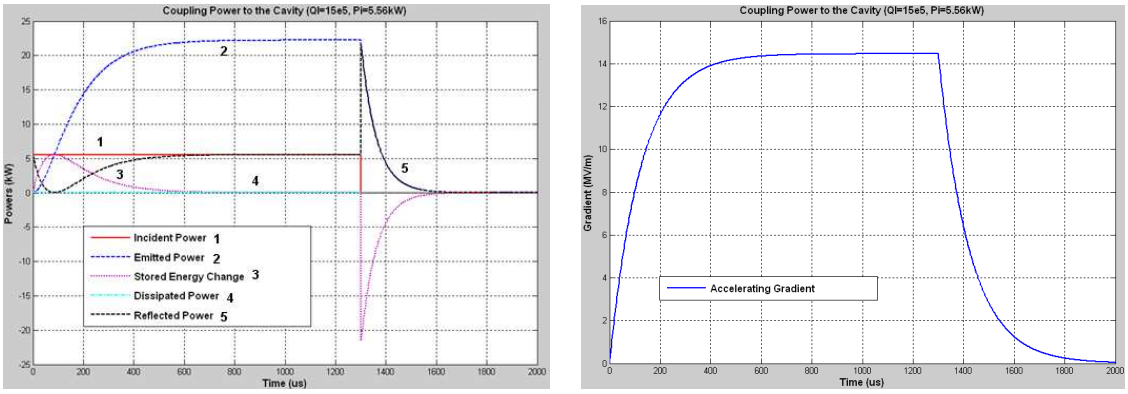

Figure 4.6. Power Level and Accelerating Gradient Curves at $Q_L = 15 \times 10^5$ and Incident Power of 5.56 kW

As shown in Figure 4.7, the reflected power changes from an almost square waveform to the classical waveform shown in above figures and the accelerating gradients are increasing to the 14.5 MV/m designated level when the frequency of incident power is closing to the cavity resonance frequency, 3.9 GHz. The equivalent circuit model including a series of lumped equivalent circuits can accurately describe the RF coupling system's operating conditions. These equations and solutions can be used to exactly calculate the SC cavity parameters, power levels, and monitor the coupling effects.

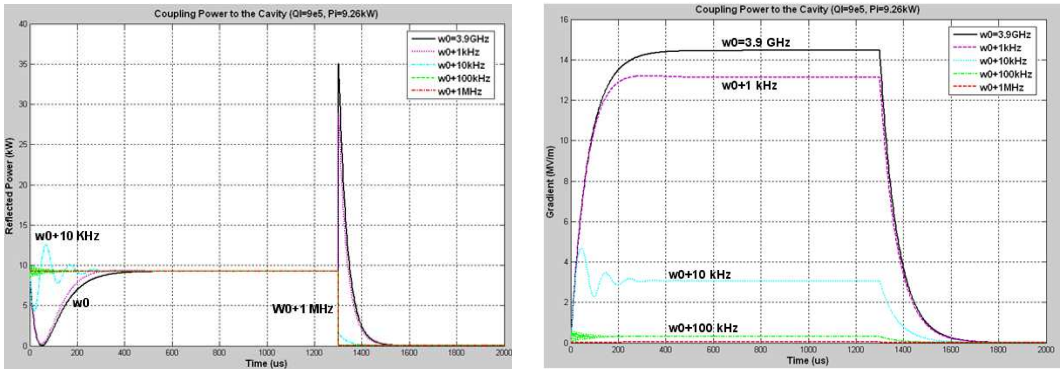

Figure 4.7. Power Level and Accelerating Gradient Curves at $Q_L = 9\times10^5$ and Incident Power of 9.26 kW, Operating off the Resonance Frequency

4.2 Required Incident Power from Klystron

A current source in parallel with the generator in the equivalent circuit model can be simply represented the beam current based on a series of observations and assumptions [55]. It is useful and important to investigate the required incident power from the generator for the coupling system with relation to the loaded quality factor and beam current [55], [58]. There are many ways to get this solution, while the easiest one is to derive from the vector diagram [55] shown in Figure 4.8 instead of from the circuit differential equation.

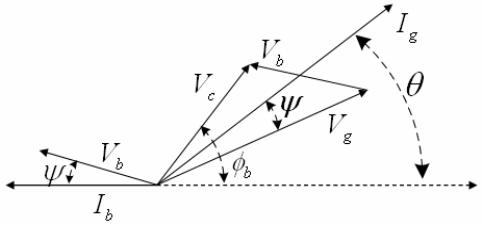

Figure 4.8. Vector Diagram of the Generator-Induced Voltage and the Beam-Induced Voltage in a Detuned Cavity

Some definitions are mentioned in advance. V_c is the combined cavity voltage, V_b is beam-induced cavity voltage, and V_g is generator-induced cavity voltage. I_b denotes the beam current and I_g is generator current, ϕ_b is the beam delay phase and $\tan\psi = Q_L(\frac{\omega_0}{\omega} - \frac{\omega}{\omega_0})$ denotes the detuning angle, respectively.

It is a simple process to write the following two equations [55] from the vector diagram,

$$V_c = V_g \cos(\phi_b - \theta + \psi) - V_b \cos(\psi + \phi_b)$$

$$0 = V_g \sin(\phi_b - \theta + \psi) - V_b \sin(\psi + \phi_b)$$

By replacing $\cos(\phi_b - \theta + \psi)$ and $\sin(\phi_b - \theta + \psi)$, and using the following equations:

$(\frac{R}{Q_0})Q_L = \frac{V_c^2}{\omega U}\frac{\omega U}{(\frac{V_c^2}{2R_L})} = 2R_L$, $V_g = \sqrt{\frac{8\beta R_L P_i}{\beta+1}}\cos\psi$, and $V_b = R_L I_b \cos\psi = 2R_L I_{b0}\cos\psi$. Here I_{b0} denotes the DC beam current and P_i is the incident power to the cavity.

Finally, we get (for heavy beam loading, $\beta >> 1$) [55]:

$$P_i = \frac{V_c^2}{4(\frac{R}{Q})\cdot Q_L}\left\{(1 + \frac{(\frac{R}{Q})\cdot Q_L I_{b0}}{V_c}\cos\phi_b)^2 + (\tan\psi - \frac{(\frac{R}{Q})\cdot Q_L \cdot I_{b0}}{V_c}\sin\phi_b)^2\right\}.$$

The required incident power from the generator for different loaded quality factors and beam currents are calculated and shown in Figure 4.9 and Table 4.1.

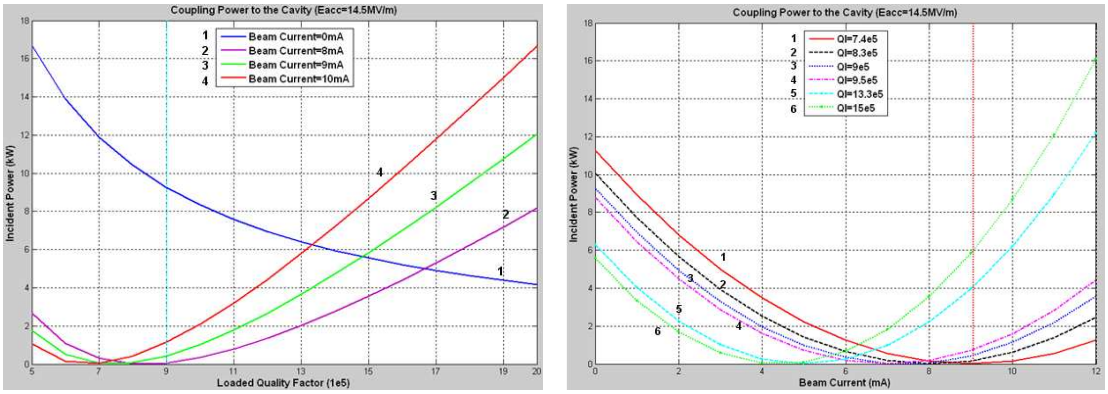

Figure 4.9. Incident Power Level as a Function of the Beam Current and the Loaded Quality Factor

Table 4.1. Required Incident Powers versus Loaded Quality Factor and Beam Current. Minus value means the phase of the incident wave is changed by 180 degrees.

Q_L	7.4×10^5	8.3×10^5	9×10^5	9.5×10^5	13.3×10^5	15×10^5
I_{b0}=0 mA	11.25 kW	10 kW	9.26 kW	8.77 kW	6.27 kW	5.56 kW
I_{b0}=9 mA	0 kW	-0.15 kW	-0.43 kW	-0.7 kW	-3.97 kW	-5.84 kW

The design of the third harmonic coupling system can couple the proper amount of power to the cavity and the beam and guarantee the minimum power consumption from the generator. The klystron can even be turned off under some special conditions. The coupling system can be easily adapted to meet the requirements of different scenario applications through adjusting the power coupler penetration length or the generator power level and phase.

4.3 The External Quality Factor

The external quality factor is a very important parameter which needs to be set to couple proper amount of power from the generator to the cavity and the beam [58]. The external quality factor as a function of the power coupler penetration length was calculated from a nine-cell cavity model built in HFSS, as shown in Figure 4.10. To calculate external quality factor, we built the following RF model. Input power coupler was 30 mm away from the end cell, which is the actual distance in operation. Power coupler tip has the same level with the cavity tube. HOM coupler was added to the input side of the cavity tube.

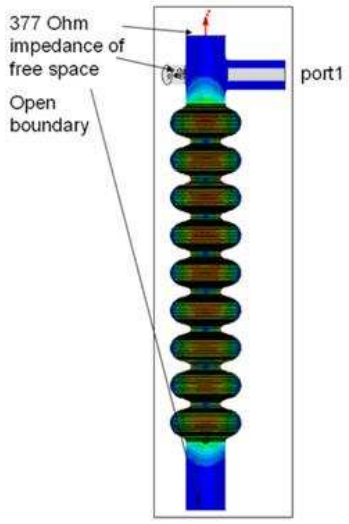

Figure 4.10. Nine-Cell Cavity Model Equipped with Power Coupler and HOM Coupler Built in HFSS

Electric field distribution in each cell on axis is shown in Figure 4.11. Quality factor can be approximately calculated from formula, $Q_e \approx Q_L = \frac{f_0}{\Delta f}$, where Δf is the

3dB bandwidth [41]. To get a higher coupling, we can insert the power coupler tip a little bit inside the cavity tube. Simulation results are shown in Figure 4.12. When the power coupler tip is flush with the wall of the cavity tube, an external quality factor of 1×10^6 is obtained. A higher coupling value can also be reached by proper adjustment of the power coupler penetration length. Minus value means the power coupler is away (outside) the wall of the cavity tube. Zero penetration length means the power coupler is just flush with the wall of the cavity tube.

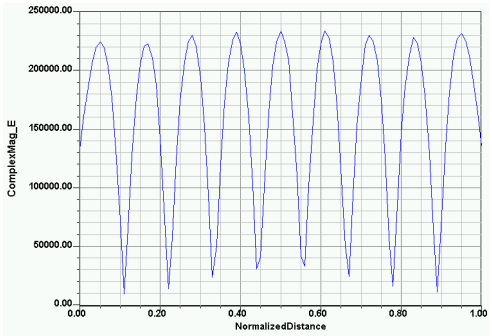

Figure 4.11. Electric Field Distribution in Nine-cell Cavity on Axis

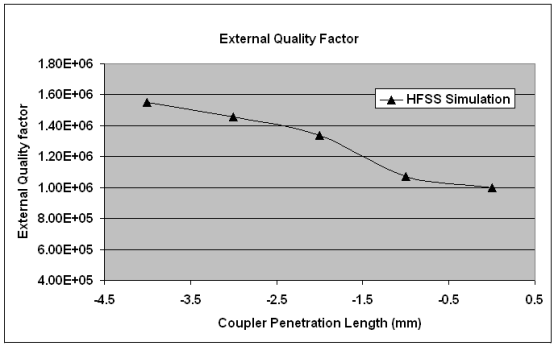

Figure 4.12. External Quality Factor versus Power Coupler Penetration Length

CHAPTER 5

CALCULATION OF MULTIPACTING

One of the major problems for accelerator components operating in vacuum is electron multipacting. Multipacting is a phenomenon of resonant electron multiplication in which a large number of electrons build up an electron avalanche. This avalanche absorbs the RF energy, leading to remarkable power losses and heating of the walls, making it impossible to raise the accelerating fields by increasing the input power [16], [17], [20]. Multipacting may cause breakdown in high power RF components such as power couplers, SC cavities, and ceramic windows [65], [75], [76]. Figure 5.1 is a picture of one-point electron trajectories for order one, two, and three. The order of a multipacting resonance is a measure of the number of full RF cycles it takes an electron to return to its original emission site. In effect, the quality factor of the SC cavity abruptly reduces at the multipacting threshold, as shown in Figure 5.2.

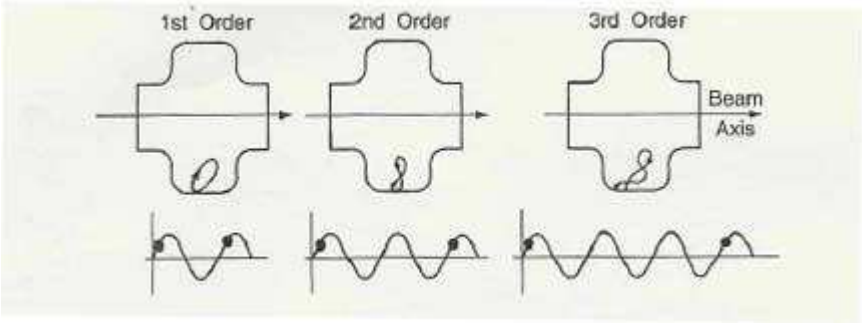

Figure 5.1. Typical Multipacting Electron Trajectories

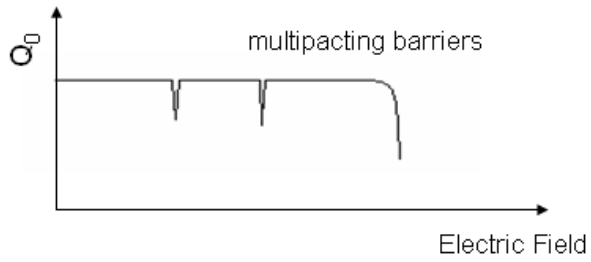

Figure 5.2. Cavity Quality Factor versus Electric Field with Multipacting

The mechanism for multipacting can be described as follows. An electron is spontaneously emitted from the surface of an RF structure and driven by the electromagnetic field. When the electron impacts the wall, it may release one or more electrons from the surfaces of the wall. The number of the secondary yield electrons depends on the impact energy of the impacting electron and the wall material characteristics at the location of the impact. Those secondary yield electrons are again accelerated by the field and yield new impacts and possibly new secondary yield electrons [4], [24], [38]. In appropriate conditions the process repeats and number of the electrons may increase greatly, leading to an electron avalanche, multipacting.

5.1 Techniques to Suppress Multipacting

There are a number of approaches to deal with multipacting. This can be done by changing the shape of the RF structure or by changing the surface properties of the structure. If operation is required at a field level that is above a multipacting resonance to the structure, problems can be avoided by changing the electromagnetic field distribution to disrupt the resonance pattern of the electrons.

5.1.1 Changing the Geometry. The best approach to avoid multipacting problems is to modify the geometry of a structure to totally avoid multipacting. For coaxial lines this could mean changing the diameter or the impedance of the line. For resonators this could mean changing the shape of the RF surface in the problematic region. Figure 5.3 shows the concept of a major change in RF resonator geometry that became standard for most SC cavities in operation today. The multipacting electrons are drifting from the iris area to the equator area and almost vanish after changing the cavity shape.

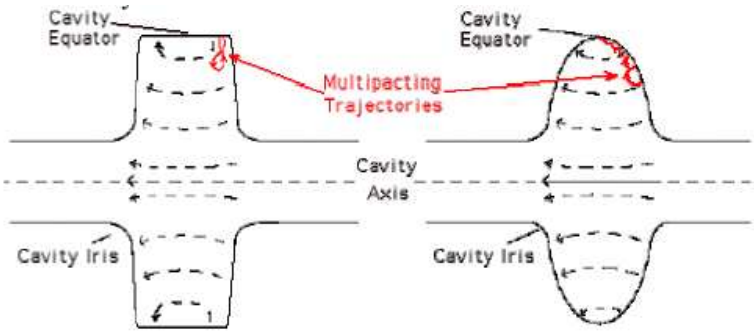

Figure 5.3. Change of the Geometry to Avoid Multipacting

5.1.2 Changing Surface Conditions. Even when resonant conditions for electrons exist, they do not automatically lead to a resonant buildup of electrons. If the secondary yield coefficient [48] of the surface at the impact energy of the electron is less than unity, no electron might be reemitted or this single electron might just be scattered off the surface. This effect opens the possibility to choose materials with a smaller secondary yield coefficient to minimize or avoid electron multiplication without having to change the geometry.

A standard technique to anti-multipacting for power couplers is Titanium (Ti) or Titanium Nitride (TiN) coating [42]. The secondary yield coefficients of Ti or TiN shown in Figure 5.4 over a wide range of impact energies are less than unity, thus not leading to electron multiplication. Since RF windows are usually made of alumina whose second yield coefficient can typically reach maximum values of 2 to 8. To reduce both surface charge buildup and the secondary yield coefficient of a window, a thin TiN coating is generally deposited at least on its vacuum side. Figure 5.5 is a picture of the cylindrical cold window for the third harmonic power coupler with TiN coated on both vacuum sides. This technology is an important method to anti-multipacting phenomena in power coupler design. Metallic surfaces often cannot be coated. For these, conditioning with modulated RF power can clean surfaces and lower secondary yield coefficients.

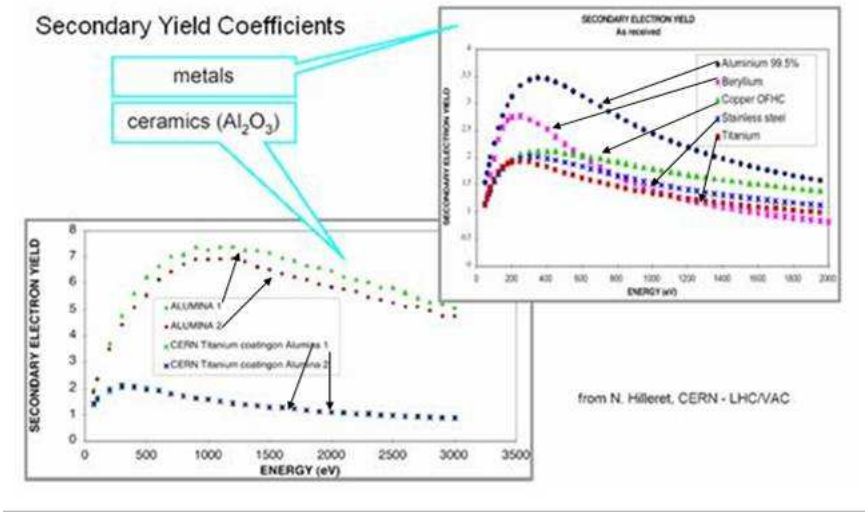

Figure 5.4. Secondary Yield Coefficients of Some Materials

Figure 5.5. Cylindrical Cold Window with TiN Coated

5.1.3 DC Field Biasing. Since resonance conditions for electrons are tightly connected to the shape of RF surfaces and the resulting RF fields, a minor change in the RF fields could also provide a disruption of the resonance paths. A standard procedure for power couplers uses the superposition of DC fields over the resonant RF fields to obtain a disruption of the resonance conditions. This technique, called biasing, usually uses DC electric voltages in the kV range for coaxial power couplers.

5.2 Multipacting Calculation

"MultiPac" is the code we used for multipacting calculation which is created from University of Helsinki for analyzing electron multipacting in the axis-symmetric RF structures with the TM_{0np} mode, such as SC cavities, power couplers, and ceramic windows [19], [36], [37]. The program finds the multipacting field levels and locates and identifies the multipacting processes. This package contains a graphical MATLAB user interface and a FEM field solver [77]. The simulations are carried out in three steps. First the program calculates the time harmonic electromagnetic fields in the given RF design. To this end an axis-symmetric FEM field solver with an automatic mesh generator and

eigen-value solver has been developed. Then the program finds the multipacting field levels by tracking electron trajectories. Thirdly the program can locate and identify the multipacting electron trajectories.

5.2.1 Third Harmonic Elliptical Cavity. Generally, multipacting will only occur in a region of the cavity where magnetic field does not vary much along the cavity wall and stable trajectories are possible. This usually occurs in the high-magnetic-field regions near the equator, where magnetic field approaches its peak value. The electrons are accelerated by the electric field while the magnetic field turns them around. By far the most successful solution to anti-multipacting was to round the cavity wall to make an elliptical cavity. In this shape, the magnetic field varies along the entire cavity wall so that there are no stable electron trajectories, as electrons drift to the equator within a few RF periods. At the equator, the perpendicular component of electric field vanishes, so that the secondary yield electrons do not gain any energy and the avalanche is not happened, which means there is no sufficient energy to create further electrons.

Multipacting calculation results of the middle cell and end cells in the third harmonic SC cavity are shown in Figure 5.6 to Figure 5.11. The enhanced counter function is the total number of secondary yield electrons after a given number of impacts (usually 20-50). From electron trajectory curves we detect electrons drift to the equator within a few RF periods and final impact energy is very low. Secondary yield coefficient of SC material, niobium, at this energy range is much less than unity so that there is no new electrons can be released from the surface, thus no electron multiplication occurred.

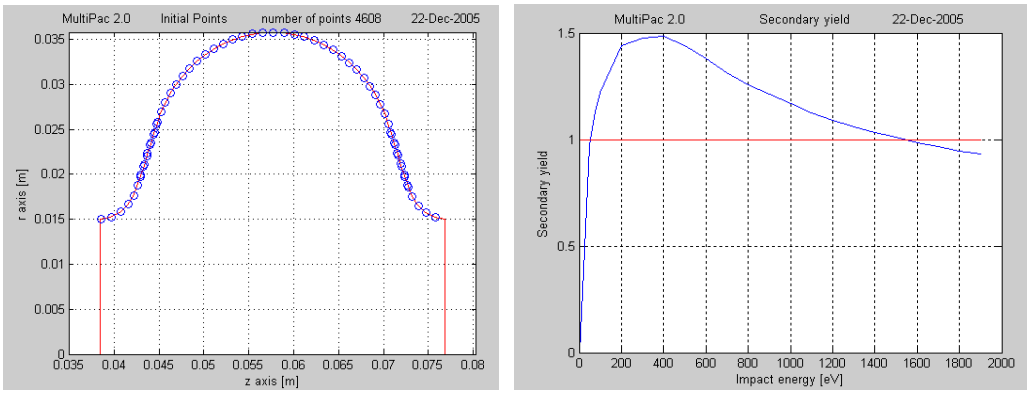

Figure 5.6. Initial Points and Secondary Yield Coefficient of Cavity Middle Cell

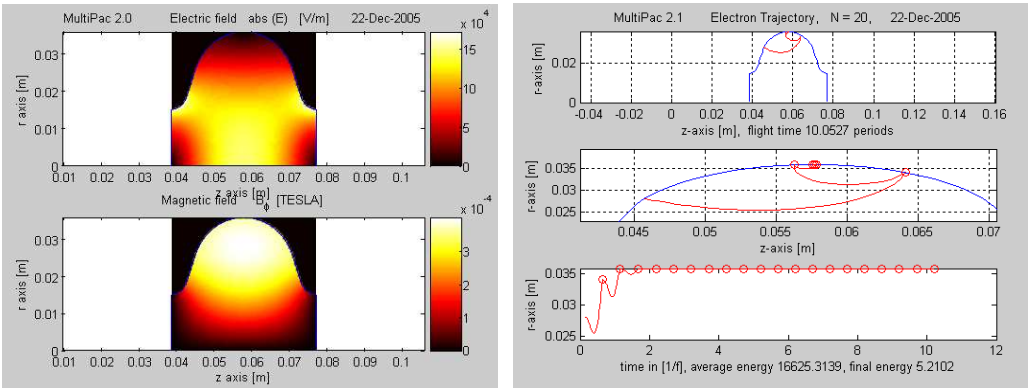

Figure 5.7. Field Maps and Typical Electron Trajectory in Cavity Middle Cell

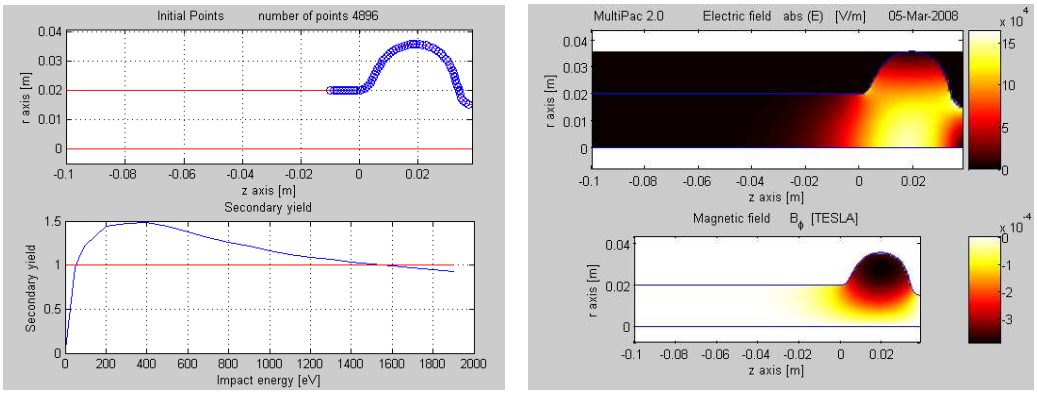

Figure 5.8. Initial Points and Field Maps in Cavity End Cell (Left Cell)

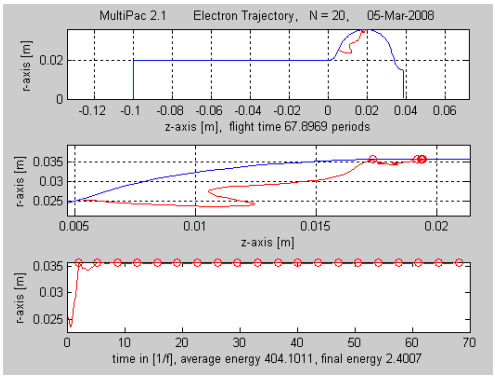

Figure 5.9. Typical Electron Trajectory in Cavity End Cell (Left Cell)

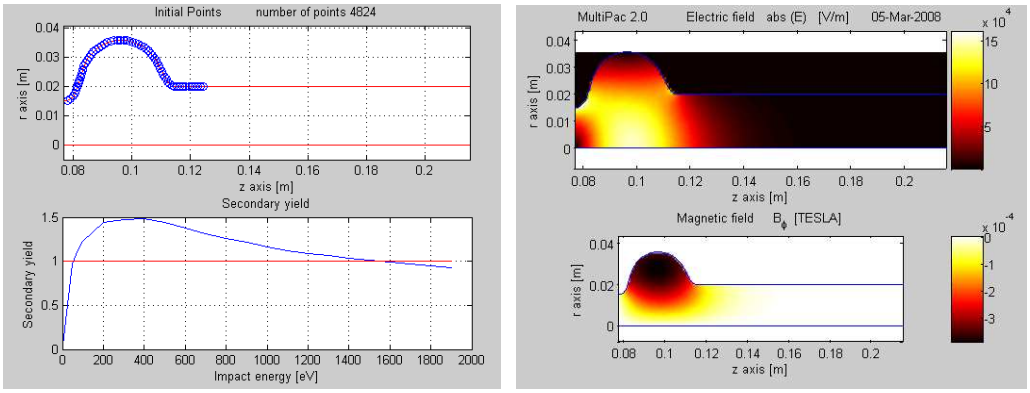

Figure 5.10. Initial Points and Field Maps in Cavity End Cell (Right Cell)

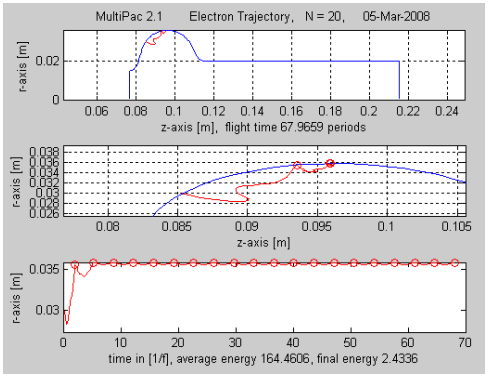

Figure 5.11. Typical Electron Trajectory in Cavity End Cell (Right Cell)

5.2.2 Coaxial Line. Usually the multipacting in standing wave (SW) in coaxial line is due to the electric field only. In fact, the powers that yield multipacting can be found by computing the trajectories at the maximum of electric field only, where the magnetic field is close to zero and hence, the repelling force $v \times B$ which can drive electrons move in radial and axial direction is minimal. Second, both one-point multipacting (from outer conductor to itself) and two-point multipacting (from outer to inner conductor and back) may occur. In the traveling wave (TW) operation the impacting location appear again close to the maximum of the electric field and the electrons are slowly traveling along with the wave as the waveform moves. Therefore, in the TW operation multipacting may appear on the entire coaxial line due to the effects of both the electric and magnetic fields.

We have calculated several cases for the power coupler coaxial line including SW and TW scenarios. We haven't found any multipacting activities during the whole operating power levels. According to the multipacting scaling law we can say multipacting power levels are shifted to high levels due to the coaxial line parameters and operating frequency. Of course there are some potential multipacting activities shown in Figure 5.12 and Figure 5.13 when power levels are higher than 400 kW in TW regime, but those levels are greatly beyond the FLASH power coupler operating levels.

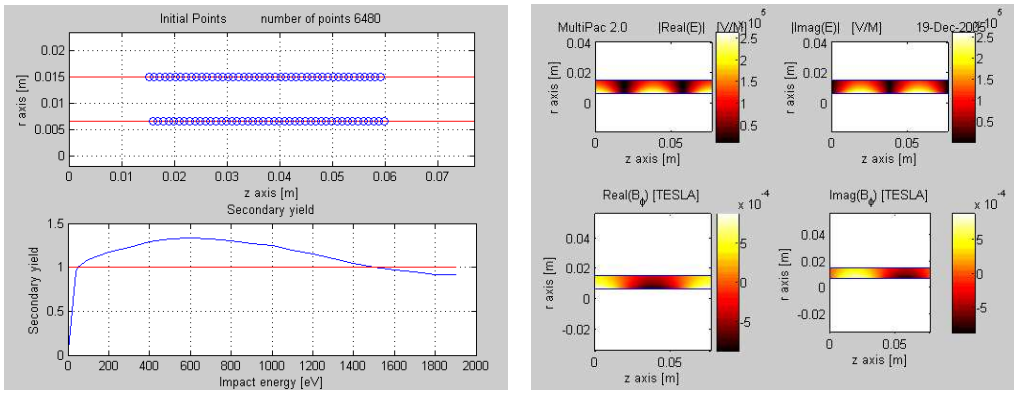

Figure 5.12. Initial Points and Field Maps of Coaxial Line in TW

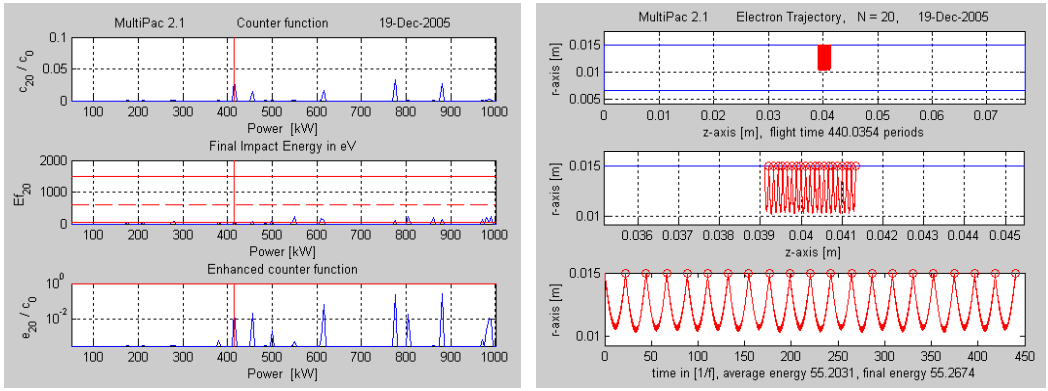

Figure 5.13. Typical Electron Trajectory of Coaxial Line in TW

5.2.3 Cylindrical Cold Window. Here we calculated three cases, mixed wave (reflection coefficient is equal to 0.875-0.484j), SW (reflection coefficient is 1 for magnetic boundary and reflection coefficient is -1 for electric boundary), and TW (reflection coefficient is equal to 0). No electron multiplication was found except for one case shown below. This is a two-point first order electron trajectory with power range from 100 kW to 150 kW in SW regime and reflection coefficient is equal to -1. Multipacting activity is fixed on warm side (input side) where inner conductor and

ceramic window is just connected as shown in Figure 5.14 and Figure 5.15. Actually this multipacting power range is still much higher than the power coupler maximum incident power level (around 15 kW) and the maximum reflected power level (around 60 kW). No multipacting issue needs to be worried about for this case.

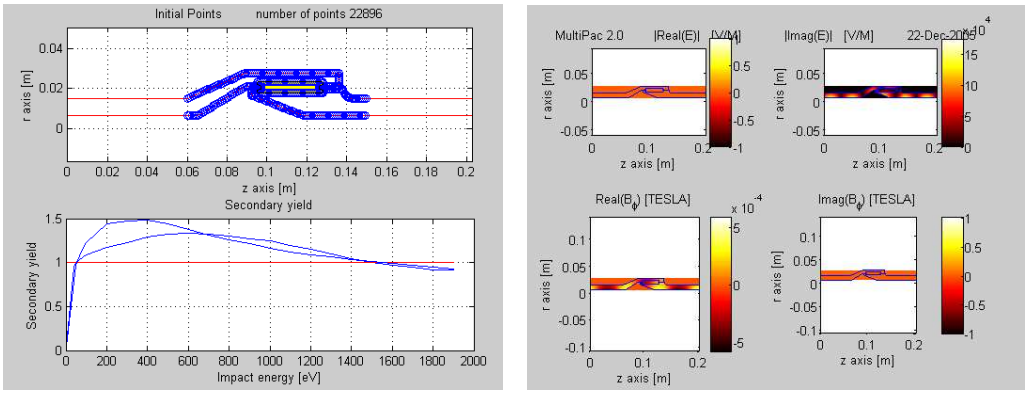

Figure 5.14. Initial Points and Field Maps of Cold Window in SW

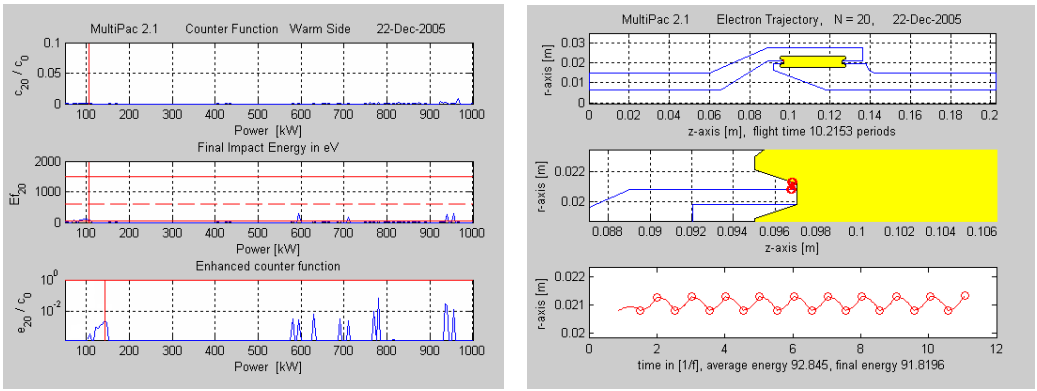

Figure 5.15. Electron Trajectory with Power Level between 100 kW and 150 kW

CHAPTER 6

THERMAL ANALYSIS

6.1 Theory of Heat Transfer

Heat tends to move from a high-temperature region to a low-temperature region. This heat transfer may occur by the mechanisms of heat conduction and radiation. Conduction is the most significant and dominant means of heat transfer in a solid. On a microscopic scale, conduction occurs as hot, rapidly moving or vibrating atoms and molecules interact with neighboring atoms and molecules, transferring some of their energy (heat) to these neighboring atoms. Denser substances are usually better conductors; metals are excellent conductors. The law of heat conduction, also known as Fourier's law, states that the heat transfer rate P through a slab or a portion of a perfectly insulated wire, as shown in the Figure 6.1, is proportional to the gradient of temperature difference. It is measured in watts. Heat flux is defined as rate of heat transfer per unit cross-sectional area, and is denoted Q, resulting in units of watts per square meter.

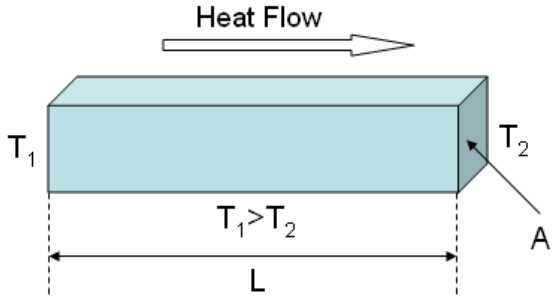

Figure 6.1. Heat Transfer Model

$$P = -kA\frac{dT}{dx}$$

$$Q = \frac{P}{A} = -k\frac{dT}{dx}$$

A is the transversal surface area, dx is the thickness of the body of matter through which the heat is passing, k is a thermal conductivity dependent on the nature of the material and its temperature, and dT is the temperature difference through which the heat is being transferred.

Figure 6.2 is showing the typical thermal conductivity curves for copper and stainless steel which are mainly used in the power coupler design. The heat conduction law forms the basis for the derivation of the heat differential equation and formula of thermal resistance.

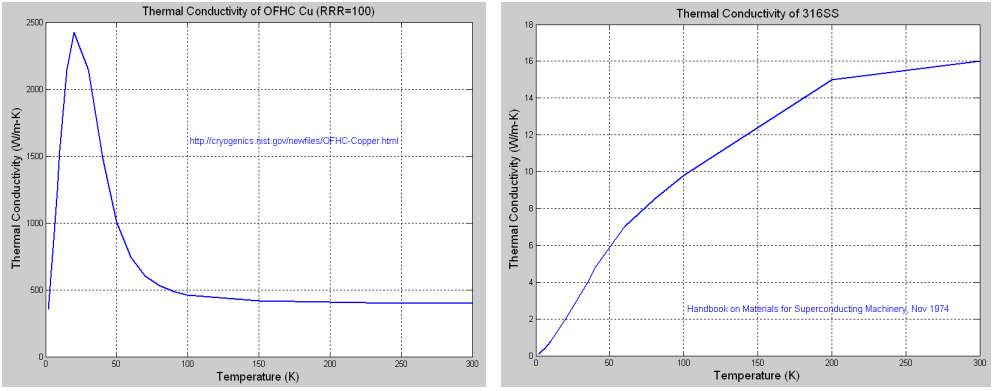

Figure 6.2. Thermal Conductivity Curves of Copper and Stainless Steel

The general heat conduction equation is $\nabla^2 T + \frac{g}{k} = \frac{\rho C}{k}\frac{\partial T}{\partial t}$. Here g is the rate of energy generation per unit volume. The unit is $\frac{W}{m^3}$. C is the heat capacity. ρ is the density of material. k is the thermal conductivity.

The general conduction equation is changed to $\nabla^2 T = 0$ (steady state) if there is no heat generation. The problem to solve is a boundary problem with internal power source and fixed temperature points as boundary conditions. $T(x) = \frac{T_2 - T_1}{L}x + T_1$ is the solution for this second order equation. Then we find the heat transfer rate and heat flux are:

$$P = -kA\frac{dT}{dx} = \frac{T_1 - T_2}{\frac{L}{kA}} = \frac{T_1 - T_2}{R_{th}}$$

$$Q = \frac{P}{A} = -k\frac{dT}{dx} = \frac{T_1 - T_2}{\frac{L}{k}}$$

The conduction thermal resistance describes the thermal properties of the materials and can be calculated:

$R_{th} = \frac{L}{kA}$ or $R_{th} = \frac{L}{A}\frac{T_2 - T_1}{\int_{T_1}^{T_2} k(T)dT}$ if thermal conductivity is temperature dependent.

When introducing additional heat generations at steady state, we can rewrite heat conduction equation to:

$$\nabla^2 T + \frac{g}{k} = 0$$

Solution of this equation is $T(x)=\frac{g}{2k}x(L-x)+(T_2-T_1)\frac{x}{L}+T_1$. And maximum temperature point can be obtained after solving equation $\frac{dT}{dx}=0$, that is $x=\frac{L}{2}+\frac{k}{g}\frac{T_2-T_1}{L}$.

It is useful to note that we put a "one-dimensional" constraint on the problem. A problem is considered one dimensional if things happen only along one dimension. This means that we are assuming that the heat going from the left side to the right side does not escape to the ambient. Well, the only way to do this is if we insulate the surface of the wire using a perfect insulator. In that case we end up with a consistent definition for the thermal resistance because all of the heat goes from T_1 to T_2. These assumptions are accurate enough to simulate and analyze the thermal properties of the 3.9 GHz power coupler within an acceptable tolerance and approximation.

6.2 Calculation of RF Power Loss

In thermal design for third harmonic power coupler, we must employ materials that can provide large thermal resistance to sustain the large thermal gradients without introducing additional RF power losses [60], [73]. In the design, inner and outer conductors are made of stainless steel with a larger thermal resistance (compared to copper) which can withhold larger thermal gradients. To obtain better RF performance, all stainless steels are copper plated in vacuum side due to the larger electrical conductivity of copper (smaller surface resistance). Meanwhile two intermediate thermal

shields including 80 K and 4.5 K degree points are included in the power coupler design to minimize the total heat loads to the cryogenic environment [8], [21].

The incident power is $P_0 = \int (E \times H) ds = (2\pi a H_a)^2 \times Z$, where $Z = 60 \ln(\frac{b}{a})$ is the coaxial line impedance, b is the radius of outer conductor, and a is the radius of inner conductor. RF power loss is:

$$P_s = P_{s\_inner} + P_{s\_outer} = (\frac{2\pi a H_a}{\sqrt{2}})^2 (\frac{1}{\sigma_a} \frac{L}{2\pi a \delta_a} + \frac{1}{\sigma_b} \frac{L}{2\pi a \delta_b})$$

$$\frac{P_s}{L} = \frac{P_{s\_inner} + P_{s\_outer}}{L} = (\frac{2\pi a H_a}{\sqrt{2}})^2 (\frac{1}{\sigma_a} \frac{1}{2\pi a \delta_a} + \frac{1}{\sigma_b} \frac{1}{2\pi a \delta_b})$$

Here $\delta = \frac{1}{\sqrt{\pi f \mu \sigma}}$ is the skin depth of copper, L is the line length, and σ is the electrical conductivity of copper.

Then we can write the peak heat flux Q and average heat flux $\overline{Q}$ expressions:

$$Q = Q_{inner} + Q_{outer} = \frac{P_{s-inner}/L}{2\pi a} + \frac{P_{s-outer}/L}{2\pi b} = \frac{0.1\sqrt{f(GHz)} P_0}{2\pi a^2 \sqrt{\sigma_a}} + \frac{0.1\sqrt{f(GHz)} P_0}{2\pi b^2 \sqrt{\sigma_b}}$$

$$\overline{Q} = \overline{Q_{inner}} + \overline{Q_{outer}} = \frac{0.1\sqrt{f(GHz)} P_0 \tau}{2\pi a^2 \sqrt{\sigma_a}} + \frac{0.1\sqrt{f(GHz)} P_0 \tau}{2\pi b^2 \sqrt{\sigma_b}}$$

$$\tau = duty \quad factor = pulse \quad length \times repetition \quad rate$$

Figure 6.3 is showing the average heat fluxes applied on the surface of inner and outer conductors due to the RF power loss. We find that most power loss is applied on the surface of inner conductor due to the higher magnetic field intensity. The higher incident power levels, the larger heat flux will be applied.

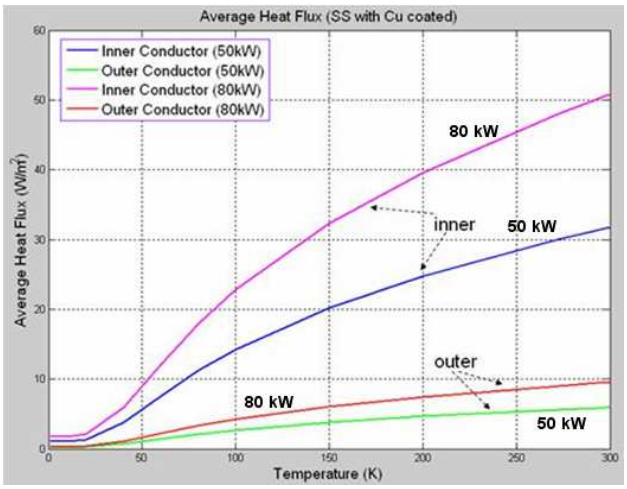

Figure 6.3. Average Heat Fluxes Applied on Inner and Outer Conductors at 1.3 *ms* and 5 Hz Pulsed Power

6.3 Thermal Analysis of the Power Coupler

The power coupler is a coaxial design with RF power transmitted in the annular region. It provides RF power to the cavity and interconnects different temperature layers in the module. Thermally, it represents a link from room temperature transmission line to the SC niobium cavity operating at 2 K. At present the analysis includes the major heat transfer mechanisms: heat conduction and RF joule heating from power loss. Therefore static and dynamic scenarios have been analyzed. 80 K and 4.5 K thermal shields are chosen to minimize the conduction and RF loss heating. Heat loads transferring to those thermal shields can't be higher than the designated limits (1 W). Figure 6.4 is a schematic diagram of the thermal model built in ANSYS. Figure 6.5 is the typical temperature map of the coupler and the ceramic cold window area at 50 kW, 1.3 *ms*, and 5 Hz pulsed power level.

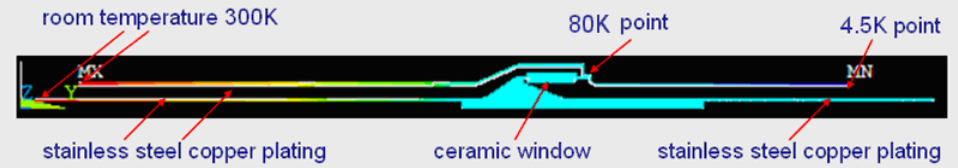

Figure 6.4. Thermal Analysis Model in ANSYS

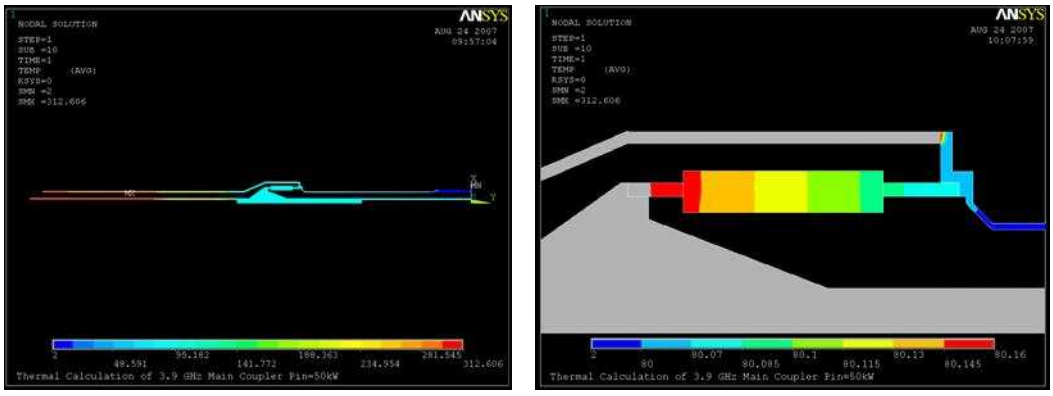

Figure 6.5. Temperature Maps at 50 kW, 1.3 *ms*, and 5 Hz Pulsed Power Level

The plating thickness of the power coupler was chosen to 15 μm for outer conductor, 30 μm for warm side of inner conductor, and 50 μm for cold side of inner conductor based on the requirements from fabricating facility. All inner and outer conductors are made of stainless steel. Ceramic windows are made of 97.5% alumina. The material properties including copper, stainless steel, and alumina are shown in Figure 6.6 and Figure 6.7.

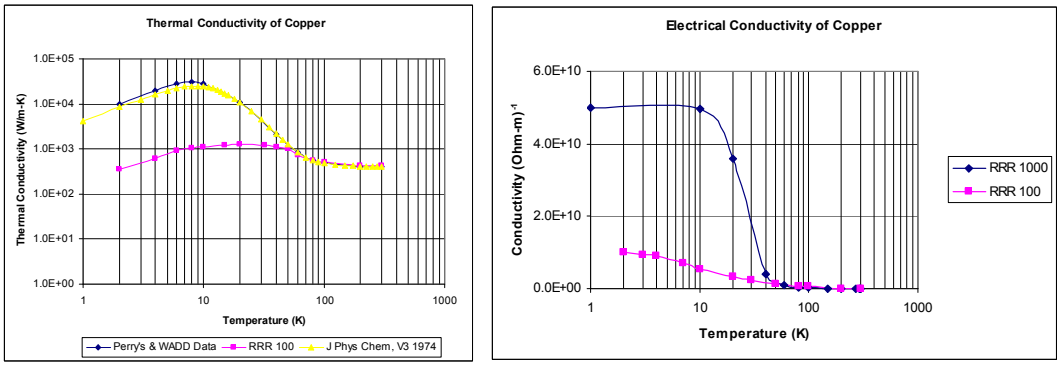

Figure 6.6. Thermal and Electrical Conductivities of Copper

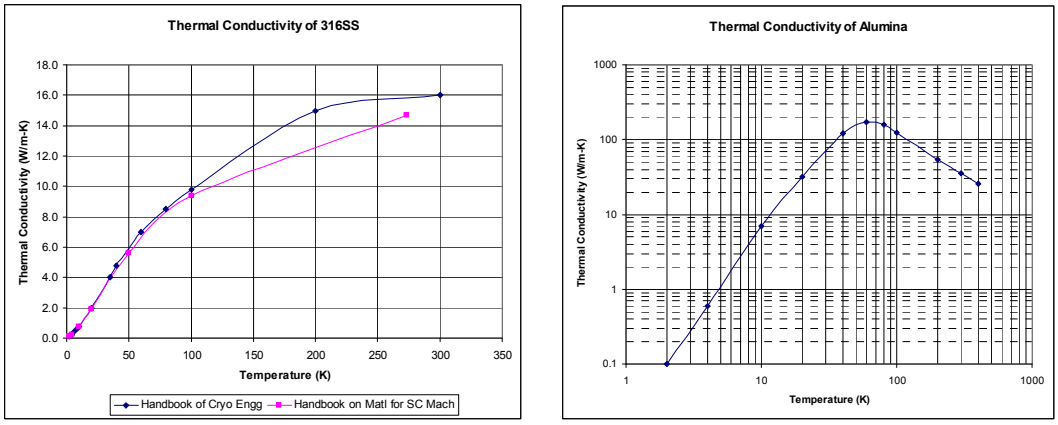

Figure 6.7. Thermal Conductivities of Stainless Steel and Alumina (Ceramic Window)

Figure 6.8 and Figure 6.9 are showing the temperature distributions along the surfaces of inner and outer conductors with different incident pulsed powers. We found that the temperature of the coupler tip which is inside the cavity tube was in the range of 80 K to 100 K depending on the incident RF power levels. The radiation heat to the SC cavity tube is very small at this temperature range and can be neglected. We have also calculated the heat loads transferring to the 80 K and 4.5 K thermal shields, as shown in Table 6.1. Please note that the heat load to the 80 K thermal shield consists of two parts,

one is from the outer conductor, and the other is from the ceramic cold window. The temperature of cold window was almost constant due to the introduction of 80 K thermal shield, which greatly reduces the possibility of window fracture. The heat loads at both 80 K and 4.5 K thermal shields were kept less than the system designated limit, 1 W. Therefore the requirements on the design of the cryostat are relatively loose.

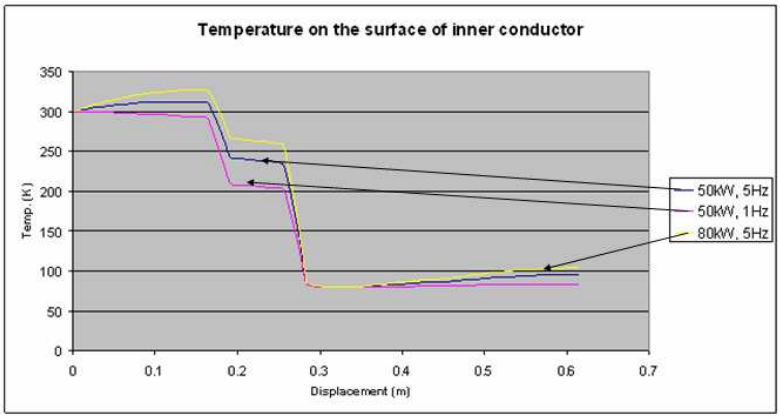

Figure 6.8. Temperature Distributions along the Surface of Inner Conductor

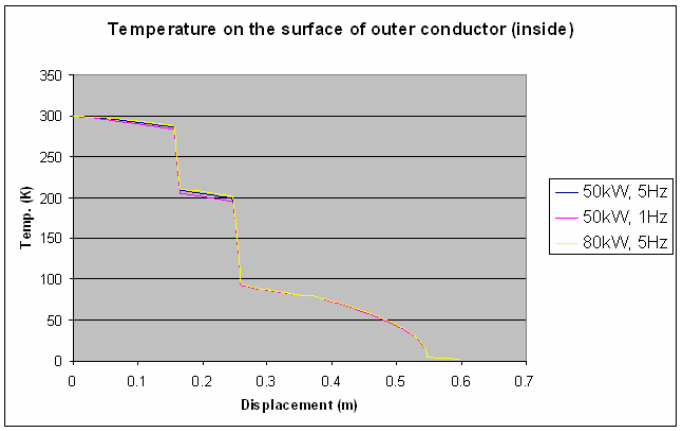

Figure 6.9. Temperature Distributions along the Surface of Outer Conductor

Table 6.1. Heat Loads at 80 K and 4.5 K Thermal Shields

Pulsed Power	80K Thermal Shield	4.5K Thermal Shield	Temp. at Coupler Tip	Temp. Gradient of Cold Window
50kW, 1.3ms, 5Hz	0.31 (outer conductor) + 0.24 (window)=0.55 W	0.19 W	95.33 K	80.147-80.096 =0.051 K
50kW, 1.3ms, 1Hz	0.29 (outer conductor) + 0.11 (window)=0.40 W	0.18 W	83.31 K	80.069-80.045 =0.024 K
80kW, 1.3ms, 5Hz	0.33 (outer conductor) + 0.34 (window)=0.67 W	0.20 W	103.74 K	80.201-80.131 =0.07 K

CHAPTER 7

HIGH-POWER TESTING AND PROCESSING

Power couplers were fabricated in industrial facilities with the collaboration of Fermilab's guidance. At first, some parts of the power couplers did not pass the quality test due to the vacuum leak problems or copper plating defects. After being repaired, all components including cold assemblies, warm assemblies, and outer conductors were returned to Fermilab and ready for high-power test. Component pictures of the power coupler are shown in Figure 7.1, Figure 7.2, and Figure 7.3. All components are made of high quality stainless steel except the rectangular waveguide, which is made of copper. All stainless steels are copper plated at least on the vacuum side for better RF performance. Return loss measurement of the power coupler at room temperature is shown in Figure 7.4. The return loss is about -19 dB at the operating frequency compared with the simulation result, -21 dB. Only 1.26% of incident power is reflected back at the input port of the power coupler.

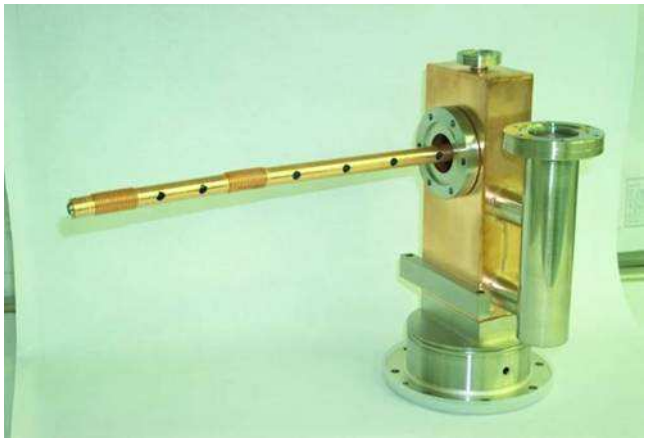

Figure 7.1. Power Coupler Warm End Assembly

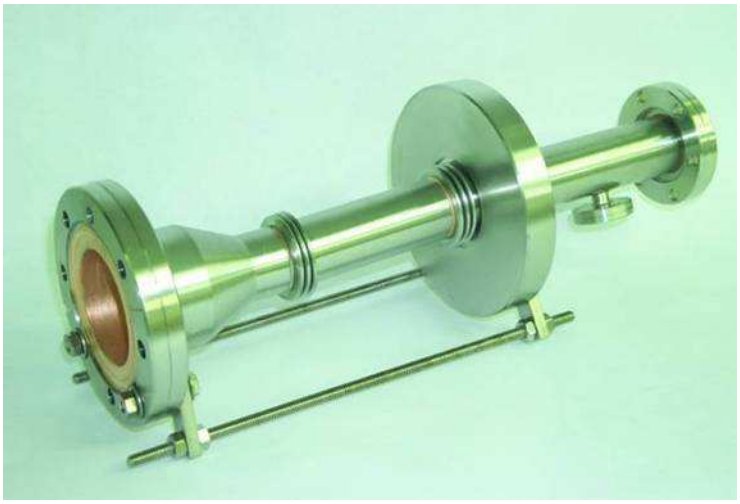

Figure 7.2. Power Coupler Outer Conductor Assembly

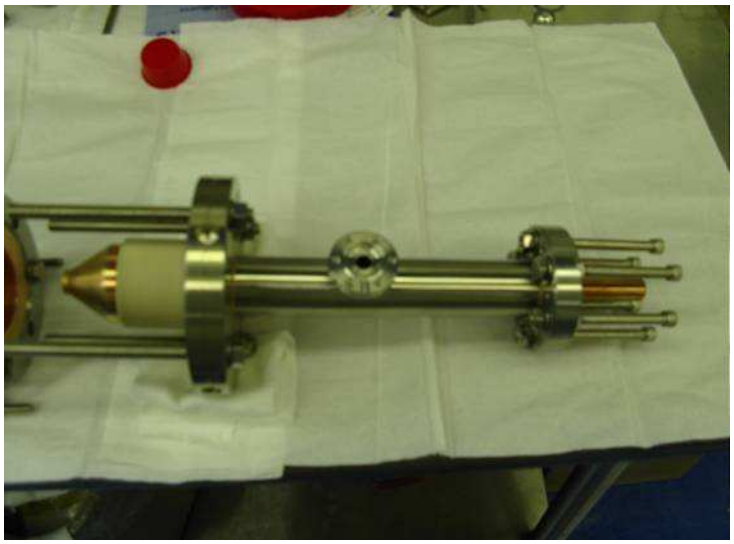

Figure 7.3. Power Coupler Cold End Assembly

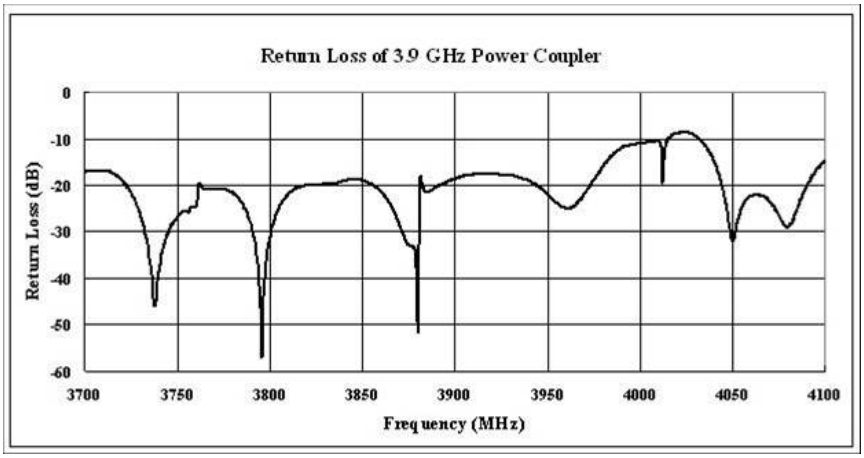

Figure 7.4. Return Loss Curve of the Power Coupler

7.1 High-Power Test Stand

It is important for the power couplers to be tested with high power prior to the assembly on a cavity cryostat since any flaws or contamination of the power couplers can degrade the cavity performance [28], [29], [66], [67], [69]. The power couplers must first be thoroughly cleaned in an ultrasonic bath. Two power couplers were assembled in back-to-back arrangement with their probes (tips) connected by a waveguide transition on a test stand shown in Figure 7.5. This design can enable the maximum power transfer between the couplers in the waveguide.

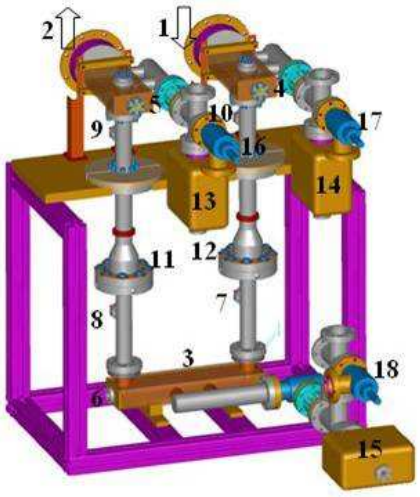

Number	Descriptions
1	Power Feed/Input Port
2	Power Load/Output Port
3	Waveguide Transition
4, 5, 6	Photomultiplier Tubes
7, 8, 9, 10	Electron Pickups
11, 12	Resistance Temperature Detectors
13, 14, 15	Vacuum Ion Pumps
16, 17, 18	Vacuum Ion Gauges

Figure 7.5. High-Power Test Stand

The whole process must include adequate protection to prevent vacuum leak, windows overheating, and arcing or sparking phenomenon. The power couplers and test stand have been equipped with various kinds of sensors including vacuum gauges, electron pickups, PMT, and RTD. Before testing the whole assembly was baked at 150 C degree for two days to remove the impurities. After being cooled to room temperature the pressure was in the $10^{-7}\ N/m^2$ range. The testing is usually done at traveling wave condition with pulsed power at the repetition rate of up to 2 Hz and under room temperature environment. The power is cycled from low to high levels, starting with short pulses (20 μs). After reaching the rated level (60-70 kW of peak power) the pulse length is doubled and the power rises again from low levels. This process will be repeated until the full pulse length of 1300 μs is reached. Coupler testing procedure is summarized in Table 7.1.

Table 7.1. High-Power Testing Procedures

Parameters	Procedures
Pulse Length (μs)	20, 50, 100, 200, 400, 800, 1300
Rep. Rate (Hz)	0.2, 0.33, 1, 2
Wave Mode	Traveling Wave
Peak Power (kW)	Maximum 80 or Klystron Output Limit
Frequency (GHz)	3.9
Number of Sensors	4 Electron Pickups, 3 Photo Detectors (PMT), 2 Temperature Detectors (RTD), 3 Vacuum Gauges

7.2 Diode Peak-Detector Calibration

Diode peak-detectors can give a reasonably accurate method of determining RF power delivered to a load for low level signals. Measured output DC voltage is simply equal to some fraction of the input peak voltage of the RF waveform. Any accurate power envelope measurement using a diode peak-detector must calibrate out the detector response in advance. Figure 7.6 shows a simplified diode peak-detector circuit model, assuming that the diode responds only to the envelope of the source voltage and that the source envelope is constant.

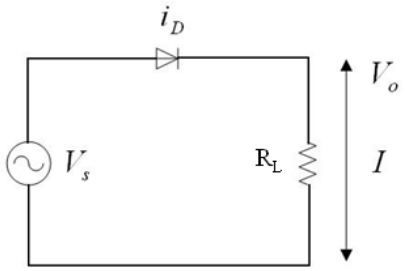

Figure 7.6. Simplified Diode Peak-Detector Model

The source voltage V_s, is assumed to be an RF waveform. The diode current-voltage relationship is approximated as $i_D = I_s(e^{\frac{v_D}{c_1}} - 1)$, where v_D is the voltage across the diode, c_1 is a physical constant, and I_s is the saturation current of the diode. Solving this equation for v_D results in $v_D = c_1 \ln(\frac{i_D}{I_s} + 1)$.

The circuit current is expressed as, $I = \frac{V_o}{R_L} = i_D$. Using the above equations, the source voltage can be expressed as, $V_s = V_0 + v_D = V_o + c_1 \ln(\frac{V_o}{R_L I_s} + 1)$.

It is obvious that the source voltage can be calculated from measured output voltage using an equation of the form

$V_s = c_0 V_o + c_1 \ln(c_2 V_o + 1)$, where c_0, c_1, and c_2 are physical coefficients.

Given a set of measurements of V_s versus V_o for an actual diode peak-detector, the coefficients of c_0, c_1, and c_2 can be determined using a generalized regression method.

The diode peak-detector calibration procedure consists of applying a known source voltage and measuring the output voltage. The experimental setup for the detectors used in the high-power testing system is shown in Figure 7.7.

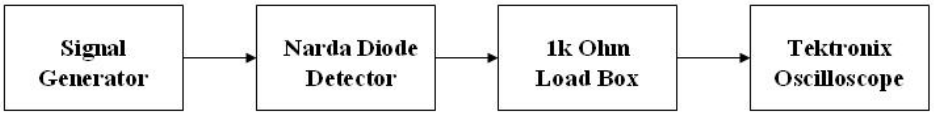

Figure 7.7. Detector Calibration Measurement Setup

The diode peak-detector circuit is made up of both the Narda diode and the 1 kΩ load. The Tektronix Scope is the actual scope used in the high power testing system. The signal generator is set to the desired operating frequency and the output response is measured as a function of the signal generator level.

The diode peak-detector calibration procedure was applied to the six detectors currently used in the coupler high-power testing system. The coefficients for each detector are shown in Table 7.2. A typical response curve is depicted in Figure 7.8 which represents the diode peak-detector for measuring klystron forward power.

Table 7.2. Diode Peak-Detector Calibration Coefficients

Diode Detector Coefficients	c_0	c_1	c_2
Klystron Drive Power	2.196	0.025	1515
Klystron Forward Power	2.207	0.024	1673
Klystron Reflected Power	2.183	0.024	1890
Input Power of Test Stand	2.185	0.023	2070
Reflected Power of Test Stand	2.205	0.025	1910
Output Power of Test Stand	2.245	0.023	1536

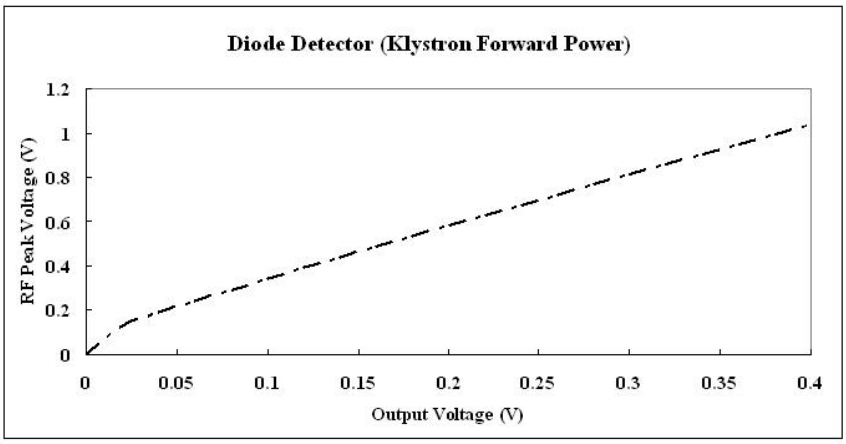

Figure 7.8. Diode Peak-Detector Typical Output Response

7.3 Testing and Processing

7.3.1 RF System Diagram. RF system diagram for high power testing is shown in Figure 7.9. A very detailed RF diagram including all components and devices is shown in Figure 7.10. Drive power, forward power, and reflected power of the klystron can be measured via directional coupler 1 and 2, respectively. Input (feed) power and output (load) power of the test stand can be measured from directional couplers 3 and 4, respectively. RF isolator is a passive device that is used to control the propagation of RF signals. It is a two-port unit that allows signals to pass in one direction while providing high isolation for reflected power in the reverse direction.

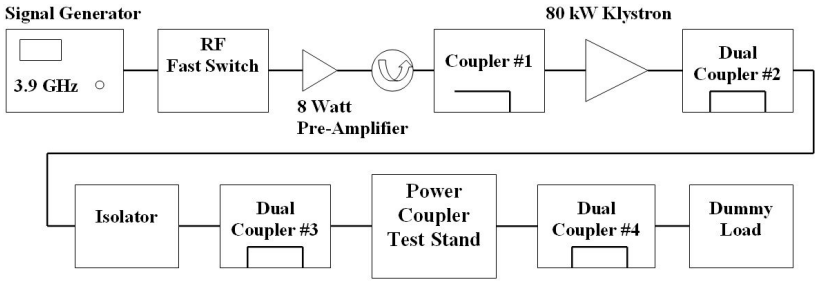

Figure 7.9. RF Diagram of High-Power Testing System

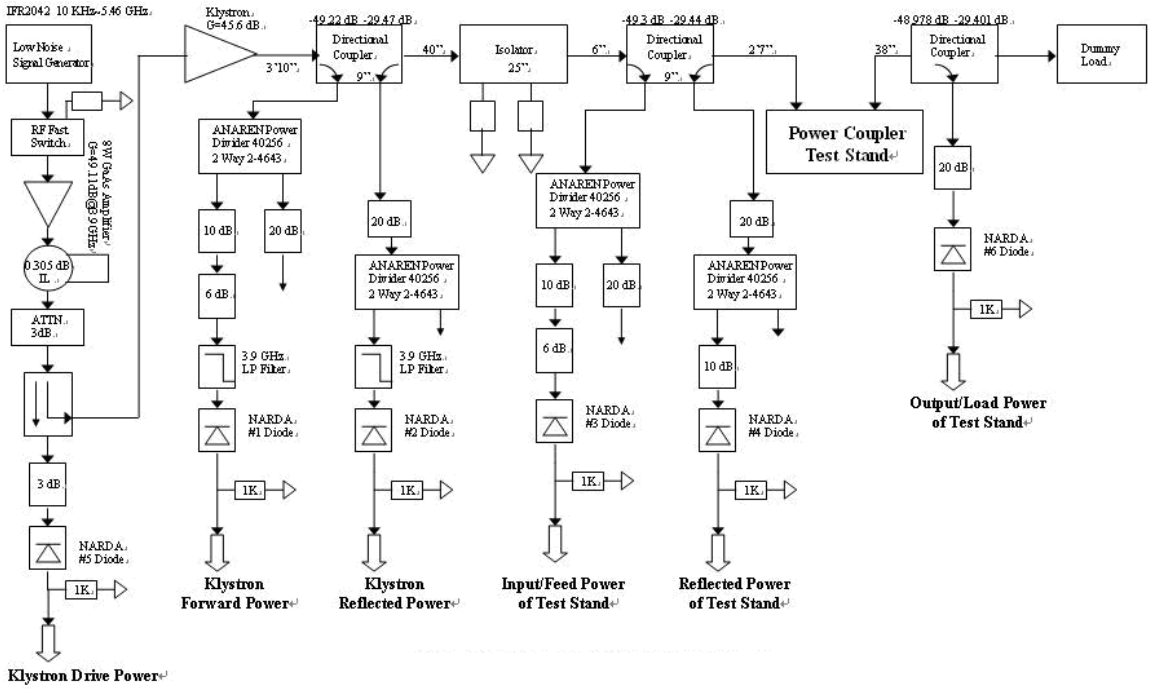

Figure 7.10. Detailed Layout of the RF Testing System

7.3.2 Klystron. Klystron is used as an amplifier at radio frequencies to produce the driving force for linear accelerators. Klystrons have the advantage (over the magnetron) of coherently amplifying a reference signal so its output may be precisely controlled in amplitude, frequency, and phase. Klystrons amplify RF signals by extracting energy from

a DC electron beam. A beam of electrons is produced by a cathode and accelerated to high voltage (typically in the tens of kilovolts), as shown in Figure 7.11. This beam is then passed through an input cavity. RF energy is fed into the input cavity at its natural frequency to produce a voltage which acts on the electron beam. The electric field causes the electrons to bunch: electrons that pass through during an opposing electric field are accelerated and later electrons are slowed, causing the previously continuous electron beam to form bunches at the input frequency. The electron bunches excite a voltage on the output cavity, and the RF energy developed flows out through a waveguide. The spent electron beam, which now contains less energy, is received by a collector. A 3.9 GHz klystron designed for the third harmonic system is shown in Figure 7.12. The klystron has a maximum output power of 80 kW at pulsed mode. The pulse length can be increased to 1300 μs and the repetition rate can reach 5 Hz.

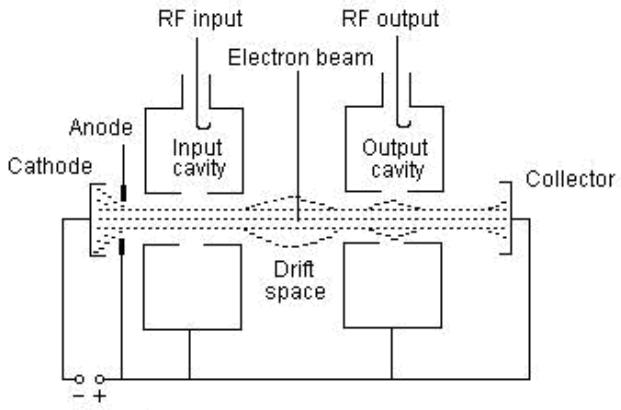

Figure 7.11. Two-Cavity Klystron Structure

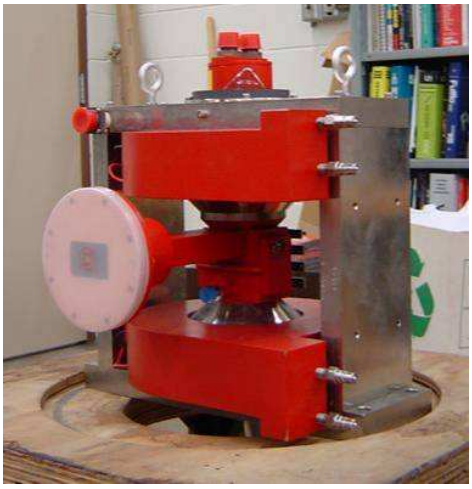

Figure 7.12. 3.9 GHz Klystron

7.3.3 High-Power Testing Results. Dressed klystron and modulator racks for high power testing are shown in Figure 7.13. Assembled power couplers in the test stand equipped with vacuum and diagnostic devices are shown in Figure 7.14.

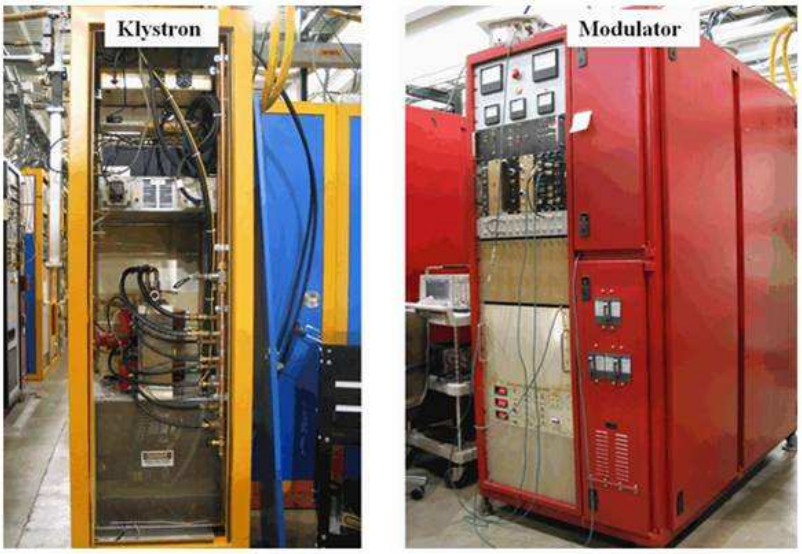

Figure 7.13. Klystron and Modulator Racks

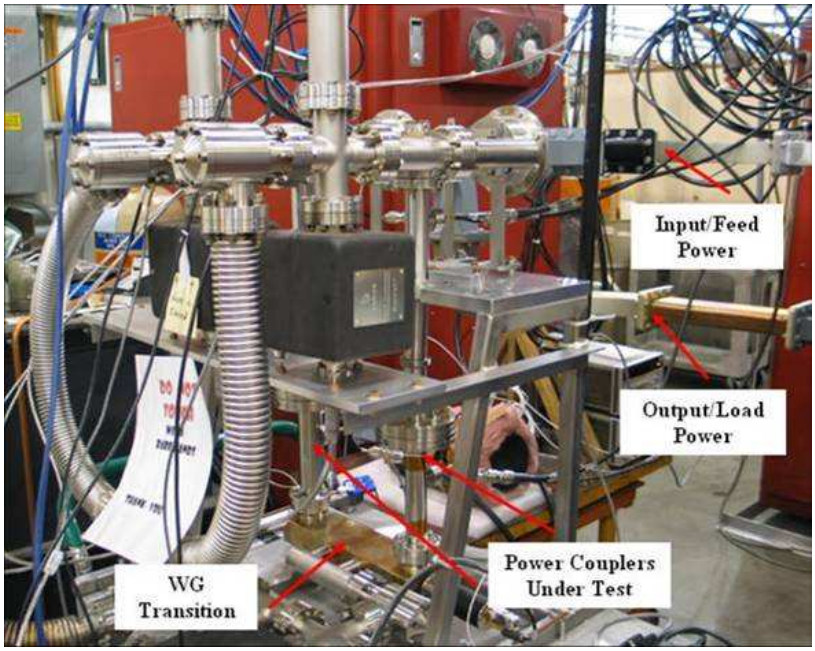

Figure 7.14. Power Coupler Test Stand Equipped with Diagnostic Devices

The power gain of the klystron was around 45.6 dB from measurements. The klystron was putting out around 64 kW of peak power at all pulse lengths before it begins to saturate. Measured power levels at different ports are shown in Figure 7.15 at 1300 μs and 800 μs pulse lengths and 1 Hz repetition rate. The maximum peak power measured at the input port of the test stand is 61 kW. Output power of 55 kW at the test stand was reached at all pulse lengths. The return loss and insertion loss of the test stand were around -18 dB and -0.6 dB, respectively, as shown in Figure 7.16.

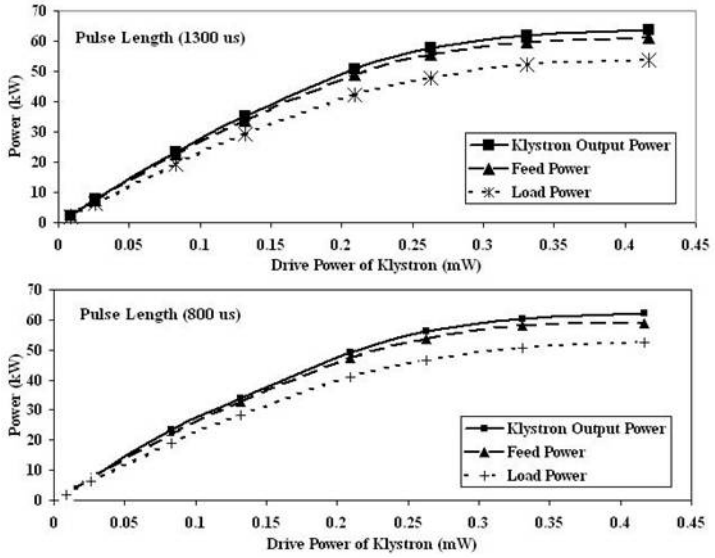

Figure 7.15. Power Levels at Different Measuring Ports

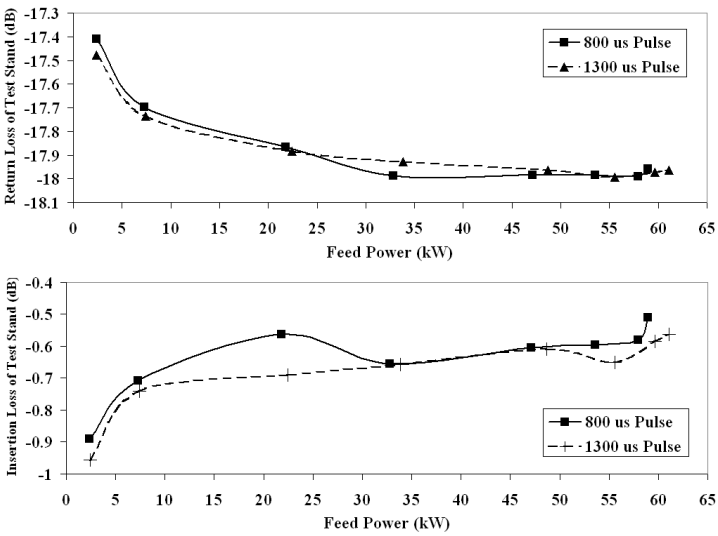

Figure 7.16. Return Loss and Insertion Loss of the Test Stand

In addition, the operation of high-power testing must include adequate protection. The power couplers in this design have been equipped with different kinds of sensors, including vacuum gauges, coaxial electron pickups, PMT tubes, and RTD sensors, to

monitor the testing effects and to act as interlocks. While running the test, no sparks and only minimal temperature and vacuum activities were observed, as shown in Figure 7.17. Two vacuum gauges (IG1 and IG3) were installed in the warm side of the power couplers. One vacuum gauge (IG2) was installed in the side wall of waveguide transition. RTD sensors (RTD1 and RTD2) were attached to the assembling flanges of the cylindrical cold windows.

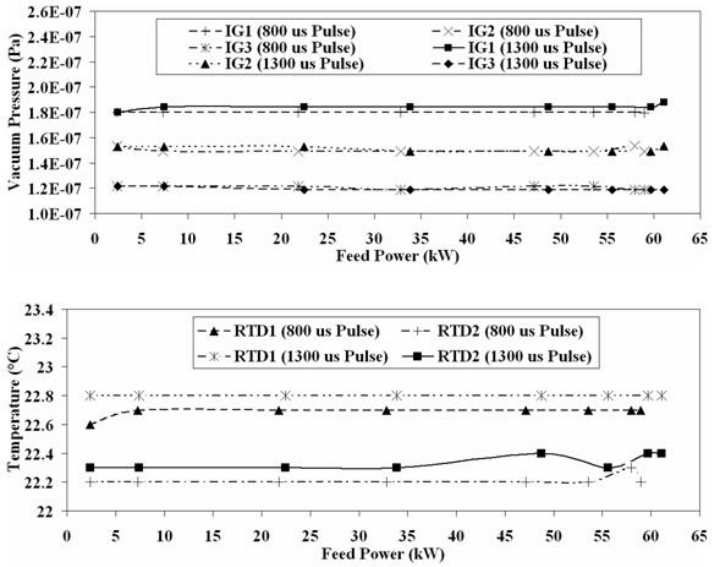

Figure 7.17. Temperature and Vacuum Readings during Testing

In conclusion, the power coupler shows an excellent RF performance and high-power handling capacity based on the results from the high-power testing and processing of the couplers. All power couplers have met the design requirements of the vacuum, RF, power-handling, power-coupling, and anti-multipacting performance. They are ready for the cryogenic test, being assembled with the dressed SC cavities in an elaborate cryostat, to mimic the real operating conditions in FLASH.

CHAPTER 8

CRYOGENIC TEST

8.1 Cavity Performance Test

During a cavity performance test, a low-power continuous wave (CW) RF voltage is applied to a SC cavity and the quality factor is measured. A high quality factor means that the cavity will better retain the energy pumped into it which is a desirable outcome from the cavity performance test process. The test thus becomes part of the qualifying process for determining that the SC cavities meet all of the extraordinary needs of the FLASH user facility [61], [62], [63]. Cavity performance test also serves to verify whether the SC cavity preparation procedures are sufficient.

In the test stand, a SC cavity as shown in Figure 8.1 is immersed in liquid helium and tested inside a vertical dewar to characterize its accelerating properties. Because the cavity essentially sits in a high bucket, it is more practical to test it in a vertical as opposed to horizontal orientation, as shown in Figure 8.2. Cooled down to a temperature of 2 K degree, we will be able to determine how high a gradient the cavity will be able to reach. This is the key factor for accelerating the particles to obtain their highest possible energies [26], [31]. The goal for the third harmonic SC cavities is an accelerating field of 14.5 MV/m with a quality factor in the order of 10^9. Typically, each cavity will spend a day inside the test stand, including the cool down and warm up period, but a test may require more time if the cavity appears to have a problem. Once the cavity completes the performance test process, it will be dressed inside a helium vessel and will continue with the next qualifying test, namely the cryogenic test of the combined coupler-cavity assembly.

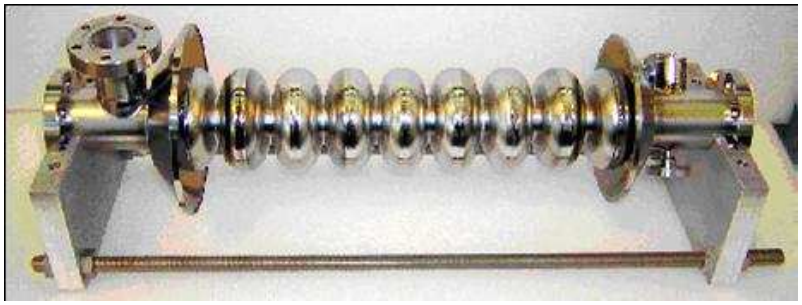

Figure 8.1. Third Harmonic SC Niobium Cavity

Figure 8.2. Cavity in Vertical Orientation

All cavities undergo a standard protocol of surface processing, including buffered chemical processing, high temperature hydrogen degasification bake, and high pressure

rinse prior to the cavity performance tests. Upon completion of fabrication, cavities are degreased and cleaned in the clean room, followed by mechanical inspection and initial RF tuning. Each cavity is tested at SC state in a shielded and interlocked enclosure. The test setup is comprised of a vertical dewar containing a single nine-cell cavity with instrumentation ports for RF input and output, vacuum and cryogenics connections, and diagnostics ports [31]. The cavity is mounted on a motorized stand so as to allow for variable input coupling. A TW tube amplifier is capable of providing up to 150 W continuous wave. The testing itself is largely a manual process and consists primarily of quality factor versus temperature (during pump down from 4 K to 1.8 K) and quality factor versus accelerating gradient measurements. Cavities may be returned for additional inside etches and high pressure rinses, as dictated by the results of testing on cavity performance.

The RF system diagram for the cavity performance test is shown in Figure 8.3. During the test we measured the time constant τ of the transmitted voltage decay curve. It is twice of the time constant τ_L of the transmitted power decay curve, which is determined by the loaded quality factor, Q_L.

$$\tau = 2\tau_L = 2\frac{1}{\Delta\omega}$$

$Q_L = \omega_0\tau_L = 2\pi f_0\tau_L = \frac{\omega_0}{\Delta\omega}$, $\Delta\omega$ is the resonance bandwidth.

The position of the input coupler was on the axis of the SC cavity. It is adjusted to minimize power reflection (almost zero), making the cavity intrinsic quality factor, Q_0, equal to the external quality factor, Q_e. The loaded quality factor Q_L is approximately

equal to half of Q_0, due to the very weak coupling effect of the field probe at the transmitted port. Some key equations used to derive the quality factors and the accelerating gradients are shown below. P_d is the cavity dissipated power, which is equal to $P_d = \frac{\omega_0 U}{Q_0} = \frac{\omega_0 U}{2Q_L}$, in which U is the cavity stored energy. The accelerating gradient can be calculated using the equation, $E_{acc} = k_t \sqrt{P_t} = k_t \times 10^{\frac{P_t(dB)}{20}}$, here k_t is a known constant obtained from FEM simulation of the structure in advance and P_t is the cavity transmitted power. The RF system is working under the critical coupling condition; maximum power can be transferred to the cavity from the power source via the input coupler on axis.

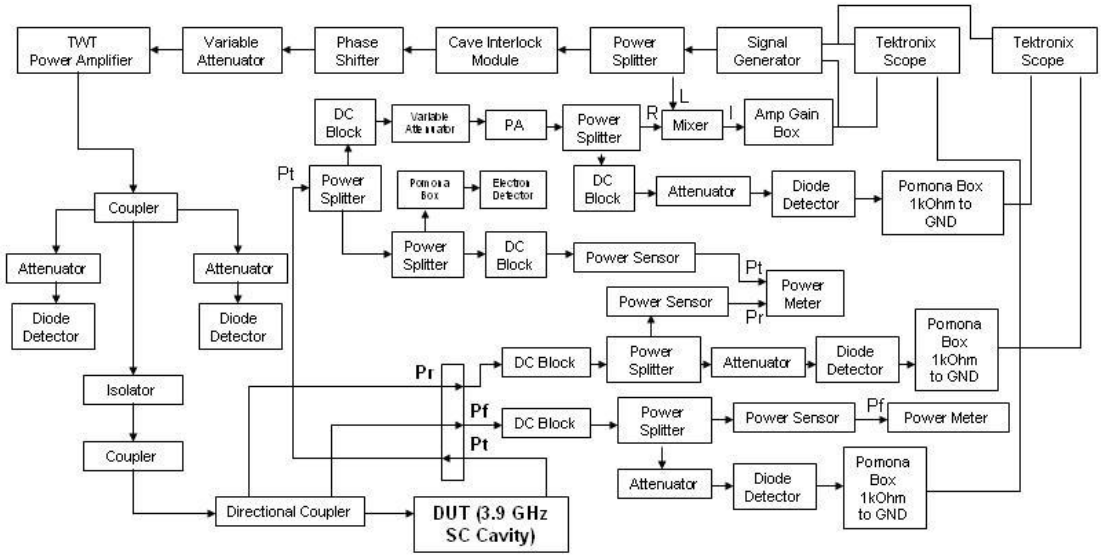

Figure 8.3. RF System Diagram for Cavity Performance Test

The measurements were made during the cool down from 4 K to 1.8 K. Typical accelerating gradients of the nine-cell SC cavity measured at π mode are shown in Figure 8.4 and Figure 8.5. The cavity was running at the gradient of 25 MV/m, limited by the power source restriction. The lower the cavity temperature, the higher will be the cavity intrinsic quality factor and power transfer to the cavity, and thus the beam. Neither X-ray nor quench was observed during the test. HOM coupler temperatures were almost constant as thermometry showed only slightly elevated temperatures, as shown in Figure 8.6.

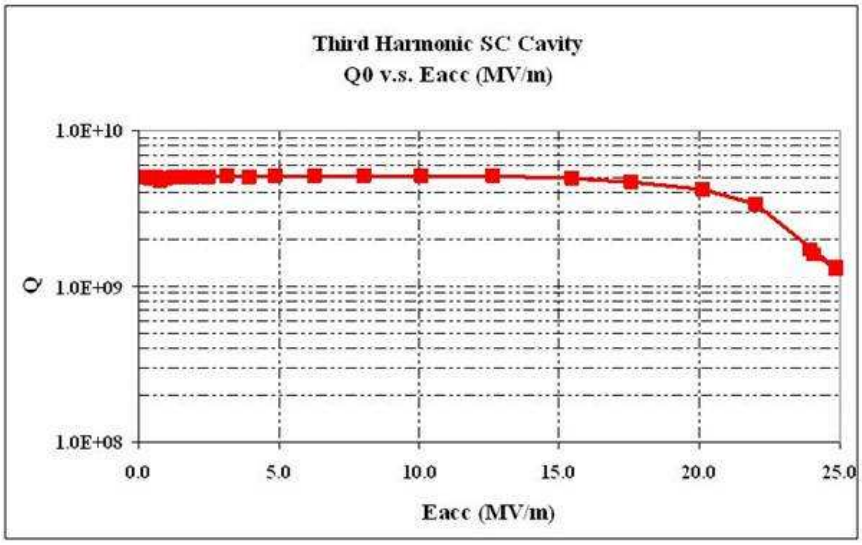

Figure 8.4. Cavity Quality Factor versus Accelerating Gradient

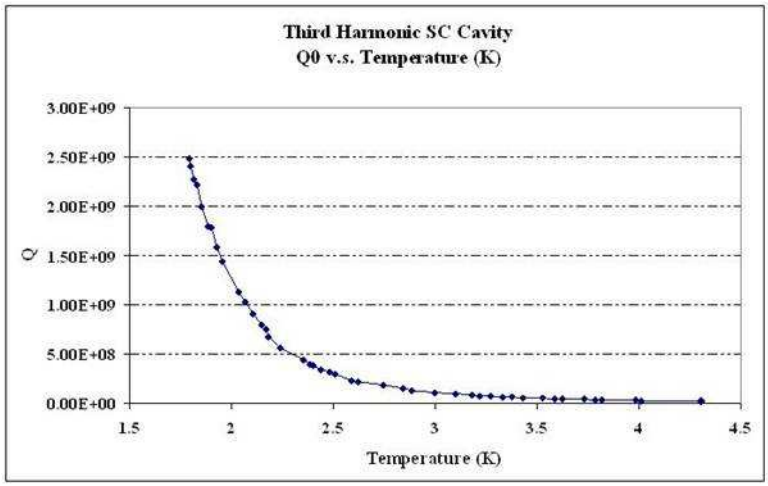

Figure 8.5. Cavity Quality Factor versus Cool-Down Temperature

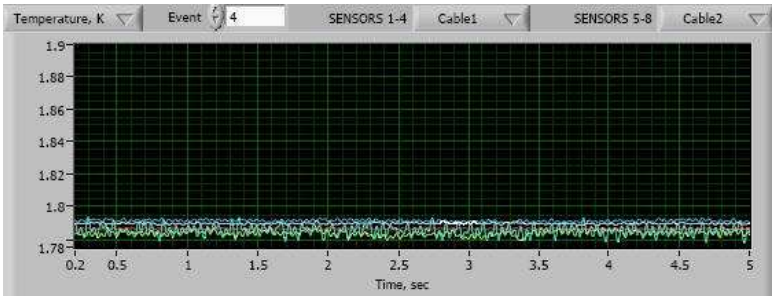

Figure 8.6. HOM Coupler Temperature Readings during Testing

8.2 Combined RF Assembly

In order to qualify for the cryogenic test, the SC cavity is first tested in a vertical test stand. After a cavity passes the performance test, it is welded inside a helium vessel and dressed with a power coupler and other components, as shown in Figure 8.7. This time, however, the cavity is tested in a Horizontal Test Stand (HTS) with high pulsed power inside a cooled cryostat at superconducting state for the cavity, in order to produce the actual conditions inside FLASH prior to incorporation of the beam.

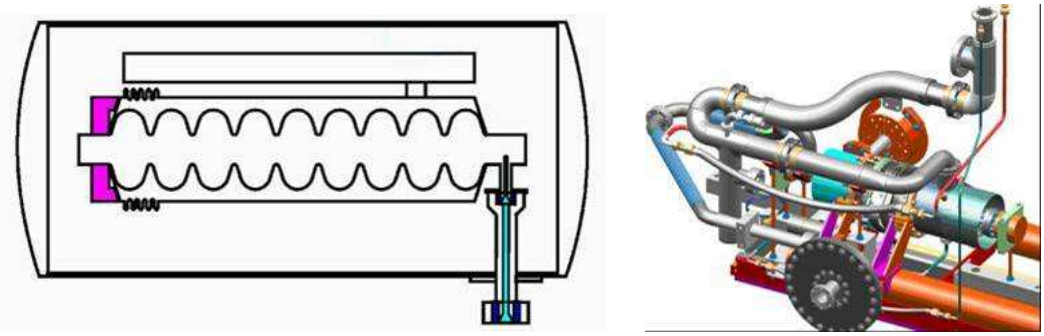

Figure 8.7. HTS for Cryogenic Test

Detailed views of the cryostat including the installation of power coupler warm and cold assemblies are shown in Figure 8.8 to Figure 8.11. In the HTS, approximately 80 kW of RF power will be switched on for about 1300 μs at a time and repeated five times per second, the same way that the FLASH will operate. As opposed to the cavity performance tests, which use lower power continuous wave RF, the horizontal test applies a much larger pulsed RF power to the cavity. This is the first time that the cavity will experience the pulsed RF power that will be similar to the conditions inside the FLASH.

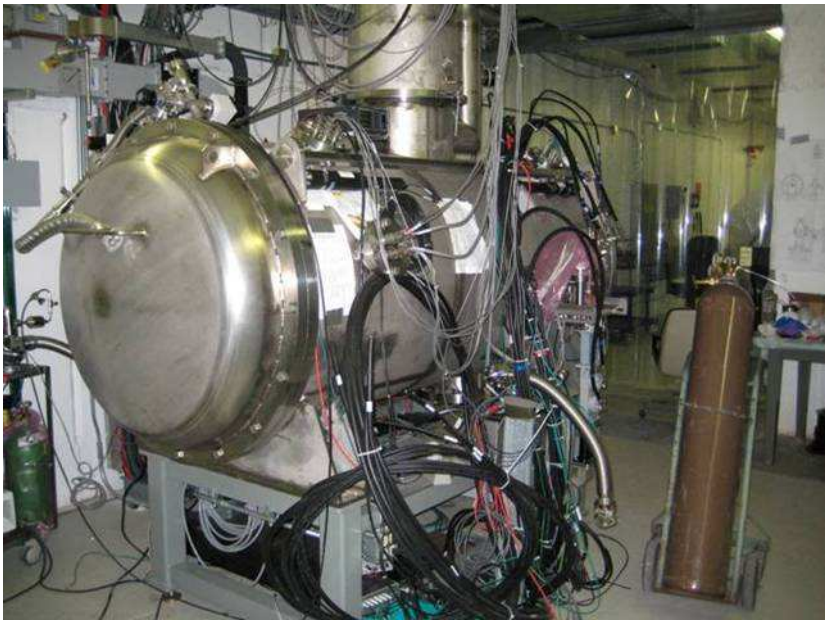

Figure 8.8. Cryostat under Testing

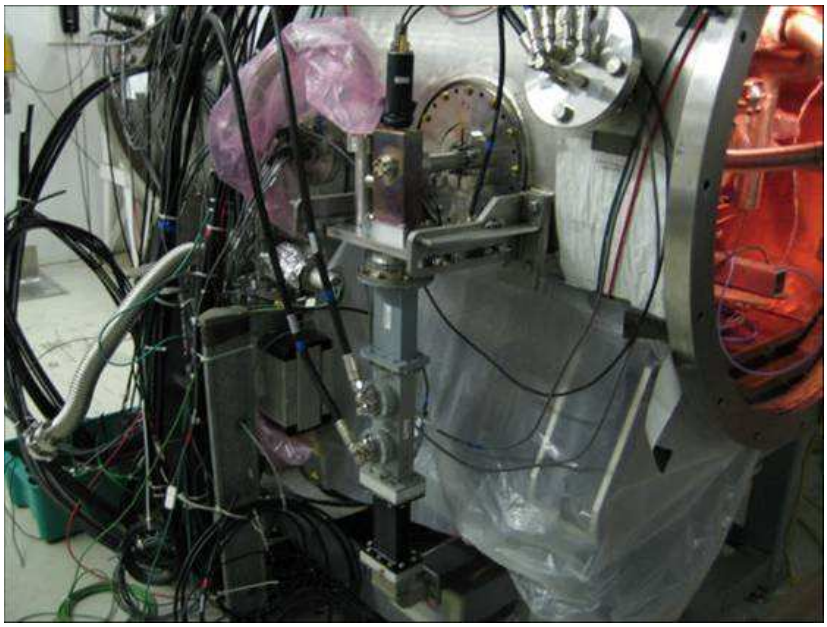

Figure 8.9. Cryostat Interfaces with the Power Coupler Warm Assembly

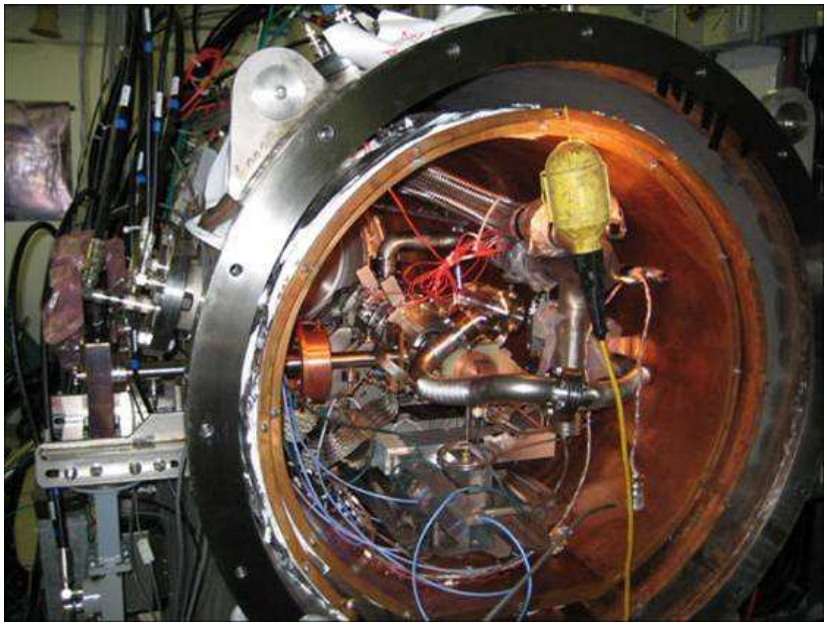

Figure 8.10. Side View of the Power Coupler and the Cryostat

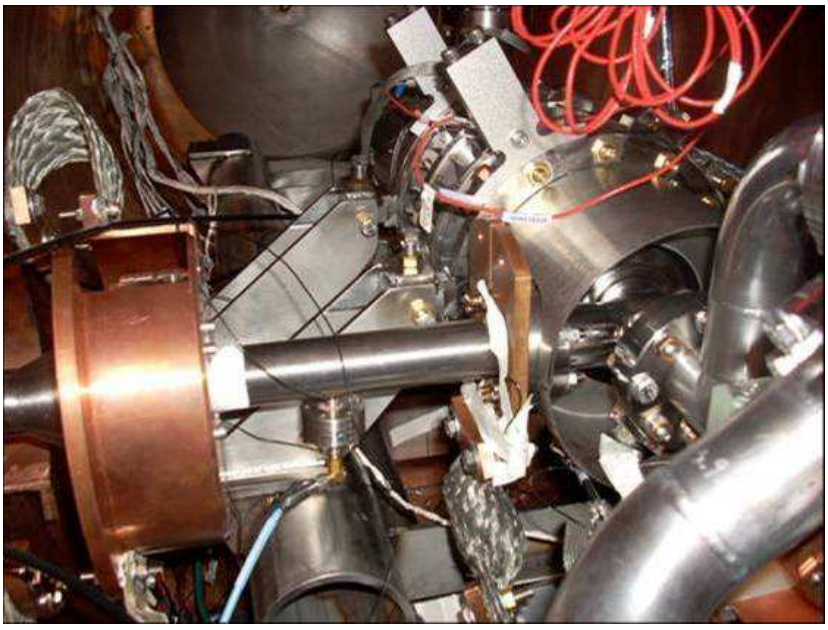

Figure 8.11. Power Coupler 80 K (Round Copper) and 4.5 K (Planar Copper) Thermal Shields

8.3 Conditioning and Cryogenic Test

8.3.1 Power Coupler Conditioning. At room temperature the cavity's resonance frequency was about 8 MHz less than the nominal 3.9 GHz operating frequency. This allows for off-resonance conditioning of the power coupler using high level pulsed power which is applied to HTS to blast away any lingering impurities and also test the whole system's qualifications and interlock functions. The conditioning sequence was performed at 1 Hz repetition rate and began with a pulse length of 20 μs . The RF power was gradually increased from zero until the maximum klystron output (60-70 kW) was reached. This power level would be sustained for one hour and then the pulse length was doubled and the power rose again from low levels. The process would be repeated until the full pulse length of 1300 μs was reached. If at any point in the sequence the pressure in the cavity or power coupler exceeds 2.7×10^{-5} N/m^2, or if electron emission in the power coupler exceeds 1 mA, the RF power will be reduced for a short period of time and then increased again. The coupler conditioning procedure is illustrated in Figure 8.12 and Figure 8.13. Minimal vacuum activity was observed during the conditioning sequence but tended to decrease with time.

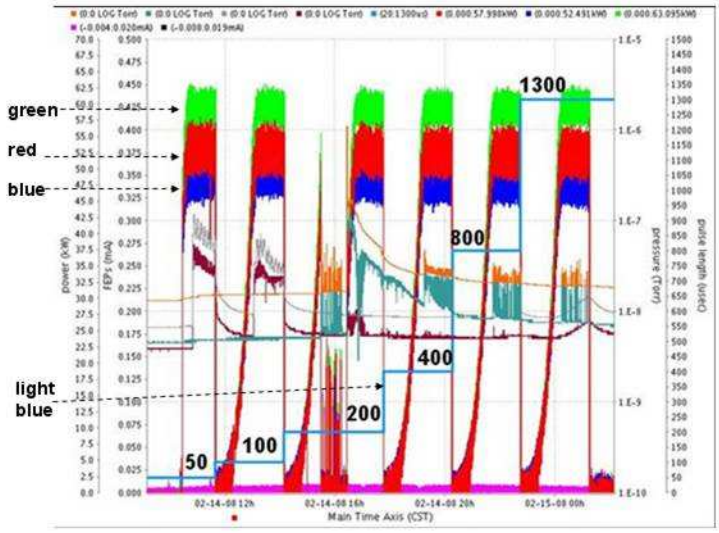

Figure 8.12. Off-Resonance Conditioning of the Power Coupler at HTS. The horizontal axis has a time span of about 17 hours. The green trace is the klystron forward power. The red trace is the cavity forward power. The blue trace is the cavity reflected power. The light blue trace is showing the pulse length (from 50 to 1300 μs) of the incident pulsed power.

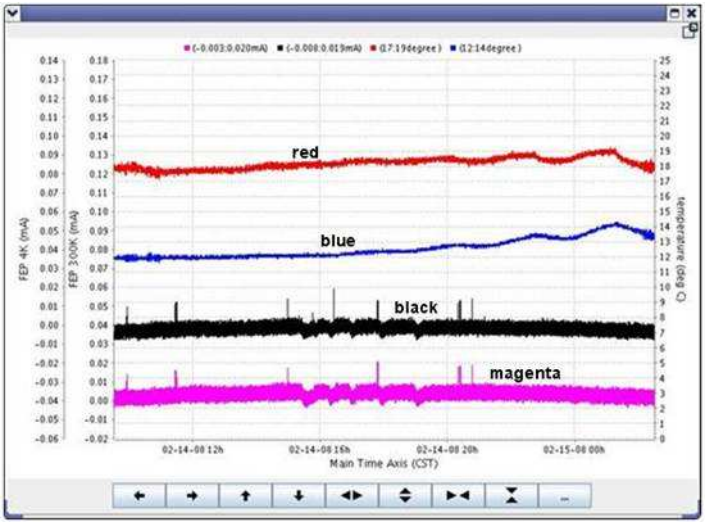

Figure 8.13. Coupler Interlock Readings during Conditioning. (red trace: temperature of warm window, blue trace: temperature of cold window, black trace: electron pickup current at cold side, magenta trace: electron pickup current at warm side)

8.3.2 Cryogenic Testing Results. For the third harmonic SC cavities, the target is to reach an accelerating gradient of 14.5 MV/m and a quality factor of 10^9 (cavity intrinsic quality factor). A lower quality factor will indicate that the cavity is losing power and thus not sufficiently efficient. The tuner motor and other components also get tested while inside the HTS, giving the cavity a thorough examination before it can graduate and become part of a cryogenic module. The maximum accelerating gradient obtained was around 24 MV/m, limited by the cavity quench, which is well above the value of 14.5 MV/m, which is specified for nominal operating condition at FLASH. Resonant frequency and the loaded quality factor on the RF system were measured using a network analyzer both before and after the system cool-down, as shown in Figure 8.14 and Figure 8.15. We can also obtain the loaded quality factor with the measurements of the power decay time constant from the cavity transmitted power curves in the field probe port at cryogenic temperature and high-power conditions, as shown in Figure 8.16.

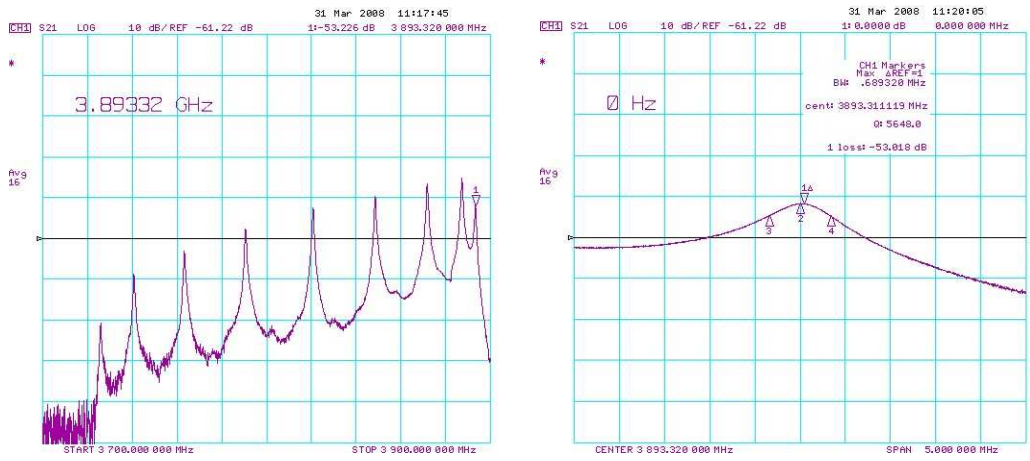

Figure 8.14. Frequency Measurements on Cavity prior to Cool-Down, The plots show the full spectrum and zoom of the π Mode.

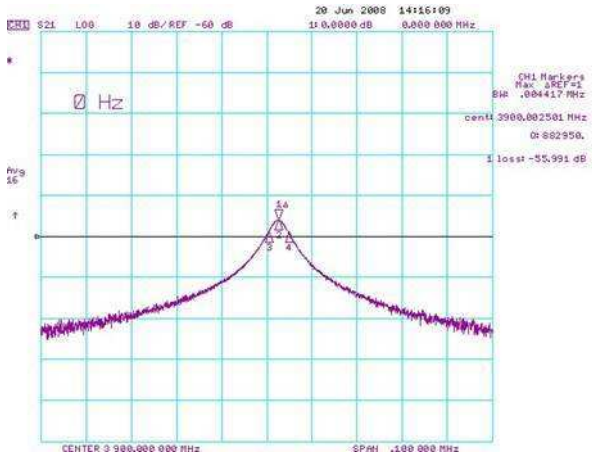

Figure 8.15. Cavity Frequency Spectrum after Cool-Down to 2 K in π Mode

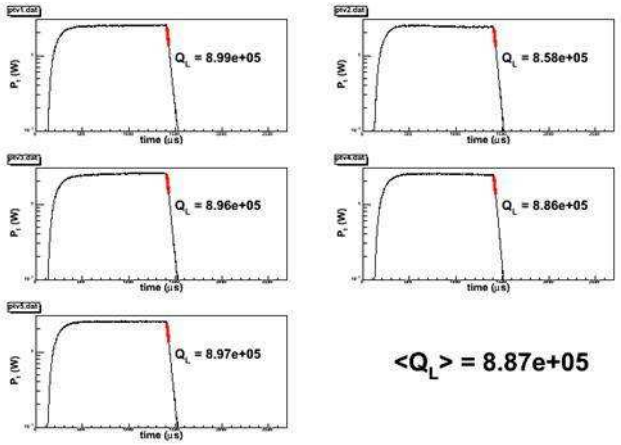

Figure 8.16. Loaded Quality Factor Calculated from Power Decay Curves at 2 K

The plot in Figure 8.14 shows the resonant transmission coefficient (S_{21}) between the power coupler and field probe ports measured at room temperature at low power level. In this scenario, the RF system operates in the under-coupled regime with a loaded quality factor of 5648. The surface resistance of the RF system is greatly reduced at cryogenic temperature, leading to a loaded quality factor of 8.9×10^5, as shown in Figure

8.15 and Figure 8.16. As such, the RF system operates in the over-coupling regime. A larger or smaller coupling coefficient, still under over-coupling regime, can be achieved if different probe penetration lengths are set. When the RF system is operated at FLASH with electron beam loading, power will be transferred to the beam, resulting in an additional loss. The RF system will be near the critical-coupling regime, leading to maximum power transfer via the power coupler for power input.

The cavity was then powered to a quench at a gradient of 24 MV/m using a pulsed wave of 1300 μs pulse length and 1 Hz repetition rate. When running at a repetition rate of 5 Hz, excessive heating of the HOM coupler was noted for gradients above 20 MV/m. Improved design of the heat sinks [25], [32] of HOM coupler to the cryogenic system has provided sufficient cooling to run the SC cavity at high gradient and 5 Hz repetition rate.

The cavity intrinsic quality factor, Q_0, was determined by measuring the dynamic heat load to the cryogenic system. Q_0 was around 2×10^9, which was in the same order as the results from cavity performance test (vertical test). The following equations are used to calculate Q_0.

$$Q_0 = \frac{(E_{acc}\cdot L)^2}{\frac{R}{Q}\cdot P_d} \text{ or } Q_0 = \frac{(E_{acc}\cdot L)^2}{\frac{R}{Q}P_{cryogenicloss}}\times dutyfactor .$$

Cavity dissipated power is $P_d = \frac{P_{cryogenic\ loss}}{duty\ factor}$ and $\frac{R}{Q} = 750 = \frac{V_{acc}^2}{\omega_0 U} = \frac{(E_{acc}\cdot L)^2}{\omega_0 U}$.

Accelerating gradient is calculated by using the equation,

$E_{acc}(V/m) = 2\sqrt{\frac{R}{Q}Q_L P_f(\omega)}(1-e\frac{-\omega\delta}{2Q_L})/L \approx 2\sqrt{\frac{R}{Q}Q_L P_f(\omega)}/L$, where δ is the pulse length.

At first, during the filling stage of the SC cavity, most power was reflected. After that, the reflected power passed through zero and reached its nonzero steady-state value, which is almost equal to the input power level since the dissipated power on the cavity surface can be neglected at the SC state. When the power was abruptly turned off at the end of the 1300 μs pulse length, the reflected power was just equal to the emitted power and exponentially decayed to zero. This power filling procedure is depicted in Figure 8.17. The maximum accelerating gradient in the cavity obtained was around 24 MV/m at a temperature of 2K with 30 kW power input from the coupler, limited by the cavity quench, which is well above the value of 14.5 MV/m accelerating gradient (9.3 kW coupler power) specified for nominal operating condition at the free-electron laser. Temperature readings of the 80 K and 4.5 K thermal shields are shown in Figure 8.18 and Figure 8.19, respectively.

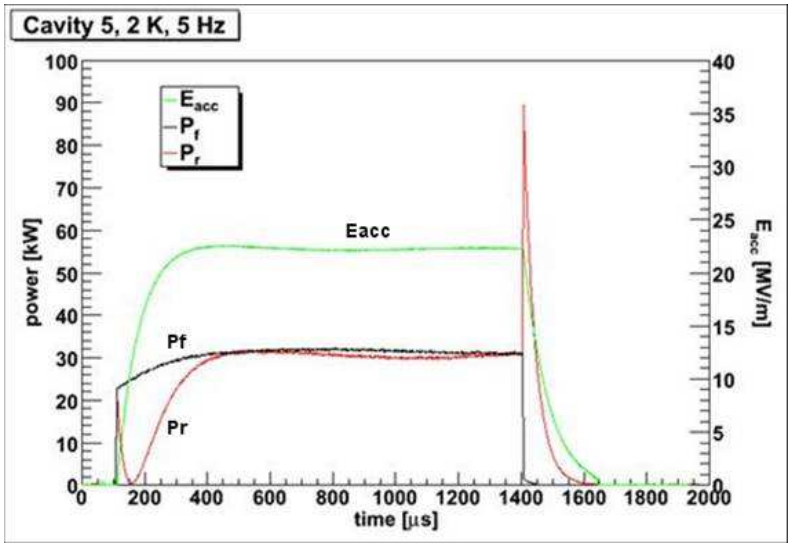

Figure 8.17. Forward and Reflected Power from the Power Coupler and the Cavity Accelerating Gradient

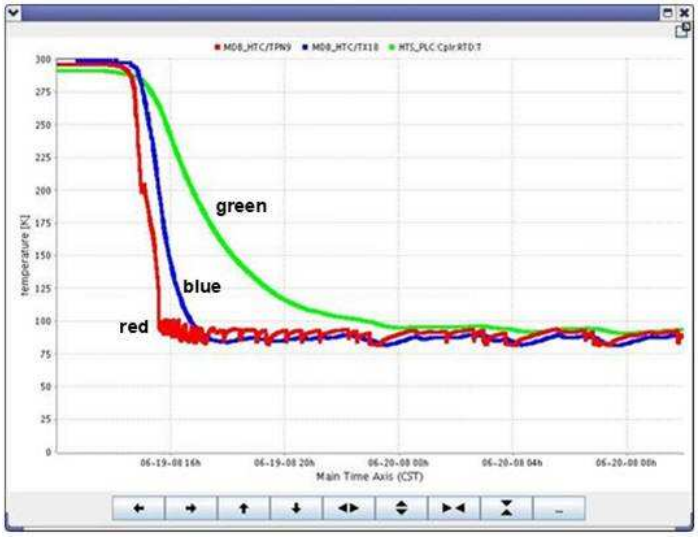

Figure 8.18. Temperature Curves Measured at Shield (Green), End-Dome (Blue), and Coupler Flange (Red) Locations at 80 K Thermal Shield

Figure 8.19. The Two Warmest Temperatures are on the End-Dome and Bottom of the 4.5 K Thermal Shield (everything else is 6.7 K or less)

Integration tests for the power coupler, SC cavity, HOM coupler, frequency tuner motor, field probe, and many diagnostic devices on a HTS were conducted at room and

cryogenic temperatures. Testing results confirmed the validity of the design, with performance data exceeding the specifications required for the intended accelerator application for FLASH, a free-electron laser for providing radiation in the vacuum ultraviolet and soft X-ray regions.

CHAPTER 9

CONCLUSION

To effectively couple microwave power into a superconducting cavity for particle acceleration application, the coupler needs to not only provide low insertion loss but also sustain high vacuum and operate between cryogenic and room temperatures. Beginning with a two-window construction with the probe orthogonal to the cavity tube, a coaxial coupler rated at 9.3 kW and 3.9 GHz for a nine-cell superconducting cavity has been successfully designed and tested. The entire coaxial coupler structure was simulated by FEM code and optimized to assure good impedance matching while keeping the total field within the coaxial structure to below the critical values for material breakdown and overheating. Before its integration with the cavity, the coupler was first processed and tested to perform at the rated power in a back-to-back configuration by gradually increasing the transmitted power and pulse length. Integration tests with the cavity were then conducted at room and cryogenic temperatures. Test results confirmed the validity of the design, with performance data exceeding the specifications required for the intended accelerator application for FLASH, a free-electron laser for providing radiation in the vacuum ultraviolet and soft X-ray regions.

In the vertical test stand the power couplers can withstand over 60 kW pulsed power with 1.3 ms full pulse length in traveling wave mode, which was well above the 9.3 kW coupler design specification. The combined RF system including the coaxial coupler, cavity, and pick-up coupler has been tested in a horizontal test stand with high pulsed power inside a cooled cryostat at superconducting state for the cavity, in order to produce the actual conditions inside FLASH prior to incorporation of the beam. The

maximum accelerating gradient obtained was around 24 MV/m, limited by the cavity quench, which is well above the value of 14.5 MV/m specified for nominal operating condition at FLASH. The power couplers designed in this way can meet the FLASH user facility's strict requirements and are suitable for numerous superconducting accelerator applications.

Power couplers for superconducting cavities are complex auxiliary systems that have significant influence on the operation of particle accelerators. To better and accurately predict the power coupler performance, especially integrated with SC cavity when operated with high energy beam bunches, it is necessary for us to include the beam effects in the simulation models and calculation procedures for the future design of the power couplers.

Much progress has been made recently in achieving high power transfer to cavities and particle beams. In the future, power couplers with higher and higher power handling capabilities will be necessary for more powerful particle machines. It will also need to reduce costs and simplify the component structure of the power couplers while still maintaining the high operating performance to make large-scale adoption of superconducting cavity technology possible. Being one of the key factors for the realization of the next generation high-energy linear colliders and particle accelerators, further efforts in coupler design and development should prove highly beneficial.

BIBLIOGRAPHY

[1] An, S., "Measurement Formulae for a Superconducting RF Cavity without Beam Load." *SNS-NOTE-AP-135 Report.* (December 10, 2004): 1-19.

[2] Arkan, T., P. Bauer, L. Bellantoni, C. Boffo, E. Borissov, H. Carter, H. Edwards, M. Foley, I. Gonin, T. Khabibouline, S. Mishra, D. Mitchell, V. Polubotko, A. Rowe, I. Terechkine, and N. Solyak. "Development of the Superconducting 3.9 GHz Accelerating Cavity at Fermilab." *Proceedings of the 2005 Particle Accelerator Conference.* (May 2005): 3825-3827.

[3] Aune, B., "Superconducting TESLA Cavities." *Physical Review Special Topics Accelerators and Beams.* 3 (September 2000): 1-25.

[4] Baglin, V., B. Henrist, N. Hilleret, E. Mercier, and C. Scheuerlein. "Ingredients for the Understanding and the Simulation of Multipacting." *Proceedings of the Chamonix X Meeting.* (January 2000): 130-135.

[5] Bauer, S., W. Diete, B. Griep, M. peiniger, M. Pekeler, J. Schwellenbach, H. Vogel, and P. Vom Stein. "Production of Superconducting 9-Cell Cavities for the TESLA Test Facility." *Proceedings of SRF 1999.* (November 1999): n.page.

[6] Belomestnykh, S., "Review of High Power CW Couplers for Superconducting Cavities." *Proceedings of Workshop on High-Power Couplers for Superconducting Accelerators.* (October 2002): 1-8.

[7] Belomestnykh, S., M. Liepe, V. Medjidzade, H. Padamsee, V. Veshcherevich, and N. Sobenin. "Development of High RF Power Delivery System for 1300 MHz Superconducting Cavities of Cornell ERL Injector." *Proceedings of LINAC 2004.* (August 2004): 694-696.

[8] Bourque R., and G. Laughon. "Thermal Analysis of a Refined APT Power Coupler and Thermal Shield and the Effect on the Cryoplant." *Proceedings of the 2001 Particle Accelerator Conference.* 2.2 (June 2001): 1083-1085.

[9] Burt, G., "Power Coupler for the ILC Crab Cavity." *Proceedings of the 2007 Particle Accelerator Conference.* (June 2007): 2212-2214.

[10] Campisi, I. E., "The Fundamental Power Coupler Prototype for the Spallation Neutron Source (SNS) Superconducting Cavities." *Proceedings of the 2001 Particle Accelerator Conference.* (June 2001): 1140-1142.

[11] Campisi, I. E., "Fundamental Power Couplers for Superconducting Cavities." *Proceedings of SRF 2001.* (September 2001): 132-143.

[12] Campisi, I. E., "State of the Art Power Couplers for Superconducting RF Cavities." *Proceedings of EPAC 2002.* (June 2002): 144-148.

[13] Champion, M., "Design, Performance and Production of the Fermilab TESLA RF Input Couplers." *Proceedings of LINAC 2004.* (August 1996): 521-523.

[14] Chel, S., "Status of the TESLA Power Coupler Development Program in France." *Proceedings of EPAC 1998.* (June 1998): 1882-1884.

[15] Chel, S., M. Desmons, C. Travier, T. Garvey, P. Lepercq, and R. Panvier. "Coaxial Disc Windows for a High Power Superconducting Cavity Input Coupler." *Proceedings of the 1999 Particle Accelerator Conference*. (March 1999): 916-918.

[16] Chojnacki, E., "Simulations of a Multipactor-Inhibited Waveguide Geometry." *Physical Review Special Topics-Accelerators and Beams.* 3 (March 2000): 1-5.

[17] Chojnacki, E., and S. Belomestnykh. "RF Power Coupler Performance at CESR and Study of a Multipactor Inhibited Coupler." *Proceedings of SRF 1999.* (November 1999): n.page.

[18] Collin, R., *Foundations for Microwave Engineering.* New York: Wiley-IEEE Press, 2000.

[19] Devanz, G., "A 2D Multipactor Simulation Code for RF Components and Accelerating Cavities." *Proceedings of EPAC 2000.* (June 2000): 1366-1368.

[20] Devanz, G., "Multipactor Simulations in Superconducting Cavities and Power Couplers." *Physical Review Special Topics-Accelerator and Beams.* 4 (January 2001): 1-5.

[21] Dohlus M., D. Kostin, and W. D. Moller. "TESLA RF Power Coupler Thermal Calculations." *Proceedings of LINAC 2004.* (August 2004): 174-176.

[22] Dwersteg, B., D. Kostin, M. Lalayan, C. Martens, and W. D. Moller. "TESLA RF Power Couplers Development at DESY." *Proceedings of SRF 2001*. (September 2001): n.page.

[23] Flottmann, K., and P. Piot. "An Upgraded Injector for the TTF FEL User Facility." *Proceedings of EPAC 2002*. (June 2002): 1798-1800.

[24] Geng, R. L., "Multipacting Simulations for Superconducting Cavities and RF Coupler Waveguides." *Proceedings of the 2003 Particle Accelerator Conference.* 1.1 (May 2003): 264-268.

[25] Gonin, I., N. Solyak, J. DeFord, and B. Held. “Multipactor Simulations in Superconducting Cavities.” *Proceedings of the 2007 Particle Accelerator Conference.* (June 2007): 2248-2250.

[26] Harms, E., T. Arkan, L. Bellantoni, H. Carter, H. Edwards, M. Foley, T. Khabiboulline, D. Mitchell, D. Olis, A. Rowe, and N. Solyak. “Status of 3.9 GHz Superconducting RF Cavity Technology at Fermilab.” *Proceedings of the 2007 Particle Accelerator Conference.* (June 2007): 2254-2256.

[27] Hayt, W. H., and J. A. Buck. *Engineering Electromagnetics.* New York: McGraw-Hill, 2001.

[28] Jenhani, H., “Preparation and Conditioning of the TTF VUV-FEL Power Couplers.” *Proceedings of SRF 2005.* (July 2005): n.page.

[29] Kako, E., S. Noguchi, T. Shishido, H. Asano, E. Chishiro, M. Matsuoka, H. Suzuki, and M. Yamazaki. “High Power Test of the 972 MHz Input Couplers for Proton SC Cavities.” *Proceedings of Workshop on High-Power Couplers for Superconducting Accelerators.* (October 2002): n.page.

[30] Kang, Y., “Electromagnetic Simulations and Properties of the Fundamental Power Couplers for the SNS Superconducting Cavities.” *Proceedings of the 2001 Particle Accelerator Conference.* 2.2 (June 2001): 1122-1124.

[31] Khabiboulline, T., “3.9 GHz Superconducting Accelerating 9-cell Cavity Vertical Test Results.” *Proceedings of the 2007 Particle Accelerator Conference.* (June 2007): 2295-2297.

[32] Khabiboulline, T., I. Gonin, and N. Solyak. “New HOM Coupler Design for 3.9 GHz Superconducting Cavities at FNAL.” *Proceedings of the 2007 Particle Accelerator Conference.* (June 2007): 2259-2261.

[33] Kijima, Y., S. Mitsunibu, T. Furuya, T. Tajima, and T. Tanaka. “Input Coupler of Superconducting Cavity for KEKB.” *Proceedings of EPAC 2000.* (June 2000): 2040-2042.

[34] Kindermann, H. P., E. Haebel, M. Stirbet, and V. Veshcherevich. “Status of RF Power Couplers for Superconducting Cavities at CERN.” *Proceedings of EPAC 1996.* (June 1996): n.page.

[35] Kostin, D., and W. D. Moller. “Status and Operating Experience of the TTF Coupler.” *Proceedings of LINAC 2004.* (August 2004): 156-158.

[36] Kravchuk, L. V., G. V. Romanov, and S. G. Tarasov. “Multipactoring Code for 3D Accelerating Structures.” *Proceedings of LINAC 2000.* (August 2000): 821-823.

[37] Kravchuk, L. V., G. V. Romanov, S. G. Tarasov, and V. V. Paramonov. "The Computer Code for Investigation of the Multipactor Discharge in RF Cavities." *Proceedings of the 1999 Particle Accelerator Conference.* (March 1999): 2799-2801.

[38] Krawczyk, F. L., "Status of Multipacting Simulation Capabilities for SCRF Applications." *Proceedings of SRF 2001.* (September 2001): n.page.

[39] Krawczyk, F. L., "Interface Issues between Superconducting Cavities and Power Couplers." *Proceedings of Workshop on High-Power Couplers for Superconducting Accelerators.* (October 2002): n.page.

[40] Li, J., E. Harms, T. Kubicki, D. Nicklaus, D. Olis, P. Prieto, J. Reid, N. Solyak, and T. Wong. "RF Design and Processing of a Power Coupler for Third Harmonic Superconducting Cavities." *Proceedings of the 2007 Particle Accelerator Conference.* (June 2007): 2265-2267.

[41] Li, J., N. Solyak, and T. Wong. "Coupling Interaction between the Power Coupler and the Third Harmonic Superconducting Cavity." *Proceedings of the 2007 Particle Accelerator Conference.* (June 2007): 2268-2270.

[42] Lorkiewicz1, J., A. Brinkmann, B. Dwersteg, D. Kostin, W. D. Moeller, and M. Layalan. "Anti-Multipactor TiN Coating of RF Power Coupler Components for TESLA at DESY." *TESLA Report 2004-02.* (2004): n.page.

[43] Matheisen, A., and F. Zhu. "Preparation of RF Power Couplers for the TESLA Test Facility." *Proceedings of Workshop on High-Power Couplers for Superconducting Accelerators.* (October 2002): n.page.

[44] Mitsunobu, S., T. Furuya, T. Tajima, and T. Tanaka. "High Power Input Coupler for KEKB SC Cavity." *Proceedings of the SRF 1999.* (November 1999): n.page.

[45] Moeller, W. D., "High Power Coupler for the TESLA Test Facility." *Proceedings of SRF 1999.* (November 1999): n.page.

[46] Moeller, W. D., "Operating Experience with Superconducting Cavities at the TESLA Test Facility." *Proceedings of SRF 2001.* (September 2001): n.page.

[47] Naito, F., "The Input Coupler for the KEKB ARES Cavity." *Proceedings of APAC 1998.* (March 1998): 776-778.

[48] Noer, R., S. Mitsunobu, Y. Kijima, and K. Saito. "Secondary Electron Yield of Nb RF Cavity Surfaces." *Proceedings of SRF 2001.* (September 2001): n.page.

[49] Orris, D., "Fast Thermometry for Superconducting RF Cavity Testing." *Proceedings of the 2007 Particle Accelerator Conference.* (June 2007): 2280-2282.

[50] Padamsee, H., J. Knobloch, and T. Hays. *RF Superconductivity for Accelerators.* Hoboken, NJ: John Wiley & Sons Press. 1998.

[51] Pozar, D., *Microwave Engineering.* Hoboken, NJ: John Wiley & Sons Press, 2005.

[52] Proch, D., "Techniques in High-Power Components for SRF Cavities-a Look to the Future." *Preceedings of LINAC 2002.* (August 2002): 529-533.

[53] Ramo, S., J. R. Whinnery, and T. V. Duzer. *Fields and Waves in Communication Electronics.* Hoboken, NJ: John Wiley & Sons Press, 1994.

[54] Safa, H., "Multiple Coupling and Beam Loading of a RF Cavity." *Proceedings of LINAC 1998.* (August 1998): 481-483.

[55] Schilcher, T., *Vector Sum Control of Pulsed Accelerating Fields in Lorentz Force Detuned Superconducting Cavities.* Hamburg: University of Hamburg, 1998.

[56] Schmierer, E. N., "Results of the APT RF Power Coupler Development for Superconducting LINACs." *Proceedings of the 2001 Particle Accelerator Conference.* (June 2001): 1110-1112.

[57] Sekutowicz, J., and R. Wanzenberg. "A Design of a 3rd Harmonic Cavity for the TTF 2 Photoinjector." *TESLA-FEL Report.* (July 18, 2002): n.page.

[58] Shemelin, V., and S. Belomestnykh. "Calculation of the B-cell Cavity External Q with MAFIA and MICROWAVE STUDIO." *SRF 2002 Report.* (2002): n.page.

[59] Shu, Q. S., "Design, Fabrication, and Testing of Novel High Power RF Input Couplers." *Proceedings of Workshop on High-Power Couplers for Superconducting Accelerators.* (October 2002): n.page.

[60] Sobenin, N. P., A. A. Krasnov, B. Y. Bogdanovich, D. A. Zavadtsev, M. V. Lalayan, V. I. Kaminsky, S. A. Belomestnykh, V. G. Veshcherevich, and A. A. Zavadtsev. "Thermal Calculations of Input Coupler for ERL Injector." *Proceedings of RulPac XIX.* (2004): 307-309.

[61] Solyak, N., "The Progress in Developing Superconducting Third Harmonic Cavity." *Proceedings of EPAC 2006.* (June 2006): 804-806.

[62] Solyak, N., L. Bellantoni, T. G. Berenc, H. T. Edwards, I. V. Gonin, and T. N. Khabiboulline. “First Results of Testing 3.9 GHz Superconducting Cavity.” *IEEE Transactions on Applied Superconductivity.* 15.2 (June 2005): 2397-2400.

[63] Solyak, N., L. Bellantoni, T. Berenc, M. Foley, H. Edwards, I. Gonin, T. Khabiboulline, D.Mitchell, and A. Rowe. “Test Results of the 3.9 GHz Cavity at Fermilab.” *Proceedings of LINAC 2004.* (August 2004): 797-799.

[64] Solyak, N., I. Gonin, H. Edwards, M. Foley, T. Khabiboulline, D. Mitchell, J. Reid, and L. Simmons. “Development of the Third Harmonic SC Cavity at Fermilab.” *Proceedings of the 2003 Particle Accelerator Conference*. (May 2003): 1213-1215.

[65] Somersalo, E., P. Yla-Oijala, and D. Proch. “Analysis of Multipacting in Coaxial Lines.” *Proceedings of the 1995 Particle Accelerator Conference.* (May 1995): 1500-1502.

[66] Stirbet, M., “Testing Procedures and Results of the Prototype Fundamental Power Coupler for the Spallation Neutron Source.” *Proceedings of the 2001 Particle Accelerator Conference.* 2.2 (June 2001): 1125-1127.

[67] Stirbet, M., “High Power RF Tests on Fundamental Power Couplers for the SNS Project.” *Proceedings of EPAC 2002.* (June 2002): 2283-2285.

[68] Stirbet, M., I. E. Campisi, K. M. Wilson, M. Drury, G. K. Davis, T. Powers, Y. Kang, K. A. Cummings, and T. Hardek. “Fundamental Power Coupler Development for the SNS Superconducting LINAC Cavities.” *Proceedings of LINAC 2002.* (August 2002): 730-732.

[69] Stirbet, M., J. Popielarski, T. L. Grimm, and M. Johnson. “RF Conditioning and Testing of Fundamental Power Couplers for the RIA Project.” *Proceedings of SRF 2003.* (September 2003): n.page.

[70] Tuckmantel, J., C. Benvenuti, D. Bloess, D. Boussard, G. Geschonke, E. Haebel, N. Hilleret, and S. Juras. “Improvements to Power Couplers for the LEP2 Superconducting Cavities.” *Proceedings of the 1995 Particle Accelerator Conference.* (May 1995): 1642-1644.

[71] Veshcherevich, V., I. Bazarov, S. Belomestnykh, M. Liepe, H. Padamsee, and V. Shemelin. “Input Coupler for ERL Injector Cavities.” *Proceedings of the 2003 Particle Accelerator Conference*. (May 2003): 1201-1203.

[72] Wanzenberg, R., “Monopole, Dipole and Quadrupole Passbands of the TESLA 9-Cell Cavity.” *TESLA 2001-33 Report*. (September 14, 2001): n.page.

[73] Waynert, J. A., and F. C. Prenger. "A Thermal Analysis and Optimization of the APT 210 kW Power Coupler." *Proceedings of LINAC 1998.* (August 1998): 950-952.

[74] Wilson, K. M., "The Prototype Fundamental Power Coupler for the Spallation Neutron Source Superconducting Cavities: Design and Initial Test Results." *Proceedings of SRF 2001*. (September 2001): n.page.

[75] Yla-Oijala, P., "Analysis of Electron Multipacting in Coaxial Lines with Traveling and Mixed Waves." *TESLA Report 97-20.* (November 1997): n.page.

[76] Yla-Oijala, P., "Electron Multipacting in TESLA Cavities and Input Couplers." *Proceedings of the 1999 Particle Accelerator Conference.* 63 (March 1999): 135-137.

[77] Yla-Oijala, P., and D. Proch. "Multipac-Multipacting Simulation Package with 2D FEM Field Solver." *Proceedings of SRF 2001.* (September 2001): n.page.